

Design and Commissioning of a Hybrid Additive Manufacturing System Combining Inkjet Deposition and Laser Powder Bed Fusion

by

Zach W. Kutschke

B.S. Mechanical Engineering, Massachusetts Institute of Technology, 2021

Submitted to the Department of Mechanical Engineering in partial fulfillment of
the requirements for the degree of

Master of Science in Mechanical Engineering
at the
Massachusetts Institute of Technology
June 2023

©Zach W. Kutschke. The author hereby grants to MIT a nonexclusive, worldwide,
irrevocable, royalty-free license to exercise any and all rights under copyright,
including to reproduce, preserve, distribute and publicly display copies of the
thesis, or release the thesis under an open-access license.

Authored by: Zach W. Kutschke
Department of Mechanical Engineering
May 12, 2023

Certified by: A. John Hart
Professor of Mechanical Engineering

Accepted by: Nicolas Hadjiconstantinou
Chairman, Committee on Graduate Students

Design and Commissioning of a Hybrid Additive Manufacturing System Combining Inkjet Deposition and Laser Powder Bed Fusion

by

Zach W. Kutschke

Submitted to the Department of Mechanical Engineering
on June 8, 2023 in partial fulfillment of the
requirements for the degree of
Master of Science in Mechanical Engineering

Abstract

Capabilities to combine multiple metal and/or ceramic materials in single components, and/or to achieve desired gradients in composition, will advance the performance of future propulsion and energy conversion systems. Multi-material and gradient capabilities have been demonstrated for metals in both powder bed and directed deposition additive manufacturing (AM) techniques; however, the dimensional fidelity and spatial precision of composition control is limited for several reasons. Here the design, fabrication, and preliminary validation of a new hybrid AM system combining inkjet printing with laser powder bed fusion (LPBF) for manufacturing compositionally graded components is presented. In the hybrid inkjet-LPBF process, a pattern of ink is deposited in a two-dimensional pattern to dictate compositionally modified regions prior to, or following, the spreading of each powder layer. Solids (e.g., nanoparticles) in the ink combine with the base powder to achieve locally controlled in situ alloying within the AM process. Key design considerations for the system including thermal isolation of the inkjet system, temperature control of the build volume (up to 500C), and atmosphere control are discussed.

Acknowledgements

Thank you to everyone in the Mechanosynthesis group for providing the support and sense of community throughout my program. I have certainly been humbled by the great minds and great work that I was fortunate enough to be around every day. A special thanks to Reimar Weißbach, Alex O'Brien, Bethany Lettiere, Emre Tekoğlu, Nicholas Diaco, Ryan Penny, Eldar Shakirov, Matteo Bugatti, & Tomasso Corbari for all of the help and support along the way.

I am also very thankful for Professor John Hart and all of his guidance and patience as I bumbled my way through the lab and my project.

THIS PAGE INTENTIONALLY LEFT BLANK

Contents

List of Figures	8
List of Tables.....	10
1. Introduction	12
1.1. Current Metal Additive Manufacturing Technologies	12
1.2. Compositional Gradients and Functionally Graded Materials	14
1.3. Key System Design Parameters.....	15
2. HAMR3 Design & Commissioning.....	19
2.1. Overview	19
2.2. Build & Supply Pistons	21
2.3. Heated Build Volume	23
2.4. Gas Knife.....	25
2.5. Inkjet Gantry.....	27
2.6. Recoater	31
2.7. Control Electronics & Software	32
3. High Temperature Inkjet Testbed.....	34
3.1. Apparatus & Experiment Overview	34
3.2. Experimental Results.....	37
4. Parameter Optimization of 316L in HAMR2	42
4.1. Background & Normalized Enthalpy	42
4.3. Optimization Process & Results	46
5. Conclusion.....	48
A. Laser Focusing & Alignment.....	49
A1. Laser Focusing.....	49
A2. Laser Alignment	51
Bibliography	53

List of Figures

Figure 1. Overview of a typical SLM system and process. Note that the inert gas flowing over the built part helps carry away spatter and plumes of material. Adapted from [14].....	13
Figure 2. A sharp conventional gradient versus a smoother transitional gradient.....	14
Figure 3. (a) The overall operation of the hybrid system, including layer-by-layer inkjet deposition; (b) layer-by-layer creation of the compositional gradient via inkjet; (c) possible application of a built-in oxygen resistant coating for additively manufacture	16
Figure 4. Overall views of HAMR3's solid model & actual construction without its enclosure.	19
Figure 5. Views of HAMR3's outside enclosure including port holes and laser window.....	20
Figure 6. (a) Overall view of the supply piston, which is nearly identical to the build piston anatomically; (b) linear bearing mount flexure used on one of the guide rails; and (c) serial flexure used to mount the ball nut to the movement stage.	22
Figure 7. Side view of the printer without enclosure, where the installed build and supply pistons may be seen.....	22
Figure 8. (a) Piston movement measurement setup; (b) change in set position versus measured change and overall error for the build & supply pistons.....	23
Figure 9. (a) Shows a cross section of the heated build volume and build piston along with the position of some of the resistive heating cartridges. The voids between the build volume and water-cooling channels as well as in the piston/screw insulation section a.....	24
Figure 10. (a) Shows one of the nozzles and the porting on the end for water cooling and the argon supply. The second argon reservoir is open at the ends for ease of manufacturing, though the mating channels help to seal this. (b) shows a cross section of the nozzle.	25
Figure 11. (a) Schematic of the gas knife control and filter setup; (b) solid model of the controller/filter assembly, with a cross section showing the internals of the cyclonic prefilter element (with the collection bin on bottom and the outlet shown at the top).	26
Figure 12. Top view of the printer without enclosure with the inkjet gantry/printhead visible over the empty build chamber.....	28
Figure 13. (a) Shows a solid model of the inkjet gantry assembly (aside from the motors, belts, and pulleys that move the y-axis), and (b) shows a cross section of the printhead.	29
Figure 14. Solid model of the recoater subassembly (pulleys, belts, and drive motors not included).	31
Figure 15. Schematic of system wide electrical controls. The heart of the system is based on a custom LabVIEW code base ran on a National Instruments cRIO FPGA with an array of DACs, ADCs, DI/Os, and other modules attached.	32

Figure 16. Sequence of events for a typical multilayer print in the system. The machine user may need to assess the nozzle function and make adjustments to its supply pressure and/or wipe the nozzle between layers.	33
Figure 17. (a) Overall inkjet system with MicroFab pressure regulator and nozzle driver, enclosure gas controls, and substrate/printhead temperature controllers. (b) Printhead, substrate heater, substrate servos, and process camera assembly; (c) cross-section of printhead; (d) individual droplet getting dispensed.	35
Figure 18. Jetting at various temperatures and the resulting SEM images showing the stability of the process. The line from (a) is roughly $47.5\mu\text{m}$, (b) is roughly $52.5\mu\text{m}$, and (c) is roughly $50\mu\text{m}$	37
Figure 19. SEM images and EDX mappings of lines jetted under different temperatures. The line pattern once again becomes faint at roughly 250C and disappears at 300C	38
Figure 20. Inkjet droplet onto 316SS substrate at 20C , (top), 220C (middle), and 250C (bottom). The green dotted line shows the path of the droplet, and the ellipse/circles indicates the droplet itself. Note that the drop bounces around after impacting the substrate.	39
Figure 21. Ink droplet onto Nb powder at 220C (top) and post deposition interaction of ink and Nb powder held at 320C (bottom). Most droplets did not appear to bounce as on the 316SS plate but rather seemed to penetrate the bed and, upon vaporizing, sent powder flying.....	40
Figure 22. DSC (dashed curve) and TG (solid curve) results obtained using the Si-NP containing ink.	41
Figure 23. Main process parameters affecting print quality in an SLM system. Adapted from [73].	42
Figure 24. (a) Front view of the HAMR2 SLM machine with the optical head in position over the laser window in the top of the enclosure. (b) Top view of an example print with 36 samples/prisms for parameter optimization. The rastered trapezoid was from a previous test raster.....	45
Figure 25. Overview of image processing sequence. (a) is the initial image with the cropped area highlighted by the pink rectangle. (b) is the portion cropped from the original image after converting it to greyscale, increasing the brightness and contrast, and applying a gaussian blur. (c) is the processed image after thresholding.....	46
Figure 26. Optical pathway setup for laser focusing & spot size characterization.	49
Figure 27. (a) Image sensor in HAMR2 chamber; (b) analyzed image with gaussian fit on the spot; (c) resulting spot size data for HAMR3 with a line of best fit attached.....	50
Figure 28. Optical pathway for alignming the incoming beam to the galvanometers.	51
Figure 29. Optical head alignment tool with calibration laser attached.....	52

List of Tables

Table 1. HAMR3 specifications and capabilities.....	20
Table 2. Nanoparticle ink formulation utilized in this study (by wt%).....	36
Table 3. Utilized inkjet parameters.	37
Table 4. HAMR2 Capabilities & Parameters.....	44
Table 5. Parameters used and varied during the optimization process	45

THIS PAGE INTENTIONALLY LEFT BLANK

1. Introduction

1.1. Current Metal Additive Manufacturing Technologies

In general, additive manufacturing (AM) processes create components through the incremental adhesion of layers, slices, or shells of the desired final form. These layers may be deposited and adhered in a number of ways, though for metal AM some of the most common processes in use are centered around powder bed fusion (PBF), direct energy deposition (DED), and/or binder jetting (BJAM).

In a PBF process the component is created layer by layer along a single direction. Metal powder is spread evenly over a region forming a new layer, and a selected region of this bed of powder is sintered or melted by a concentrated energy source such as a laser or electron beam. After forming a layer of the component, another layer of powder is spread on top to provide more material and the process is repeated until the component is finished [1], [2]. BJAM is essentially a category of PBF where the component is still created in a layer by layer fashion along a single direction, though selective regions of powder are adhered together by jetting a polymeric adhesive/binding agent on them as opposed to fusing/melting the region with a laser or electron beam. Typically after printing using BJAM, the “green” part may undergo debinding and sintering to enhance its mechanical properties [3]–[5]. Post-sintering, BJAM parts will normally undergo significant shrinkage and warping due to the material becoming denser/fusing together. These deformations can usually be predicted/analyzed and partially accounted for in the printing process to counteract spatial inaccuracy post sintering, as in the Live Sinter program established by Desktop Metal [6]. In a DED process material is fed directly to the component in the form of a powder stream or wire and is simultaneously melted to the build with a laser, electron beam, or plasma arc. Slices of material may be added along nearly any direction given that material is added locally and that the entire component doesn’t need to be submerged in a bed of powder. The resulting parts may be made much more quickly than in PBF processes, but typically with less spatial accuracy and resolution [7]–[9].

Selective laser melting (SLM) is a prominent PBF process as it tends to have greater accessibility and a wider selection of proven feedstock materials than something like electron beam melting (EBM) processes [10], [11]. EBM in particular is generally coarser, is limited in total build volume by the need to have the parts under vacuum for the duration of the print, and

has gained less general use than SLM. SLM also tends to produce parts with better dimensional accuracy and finer microstructures than selective laser sintering (SLS), EBM, DED, and BJAM processes [12], [13]. SLM systems mainly consist of a laser (or lasers) which is scanned across a powder bed with a constant spot diameter. This is typically achieved with a set of galvanometers which direct the laser through a scan lens (such as an f-theta lens).

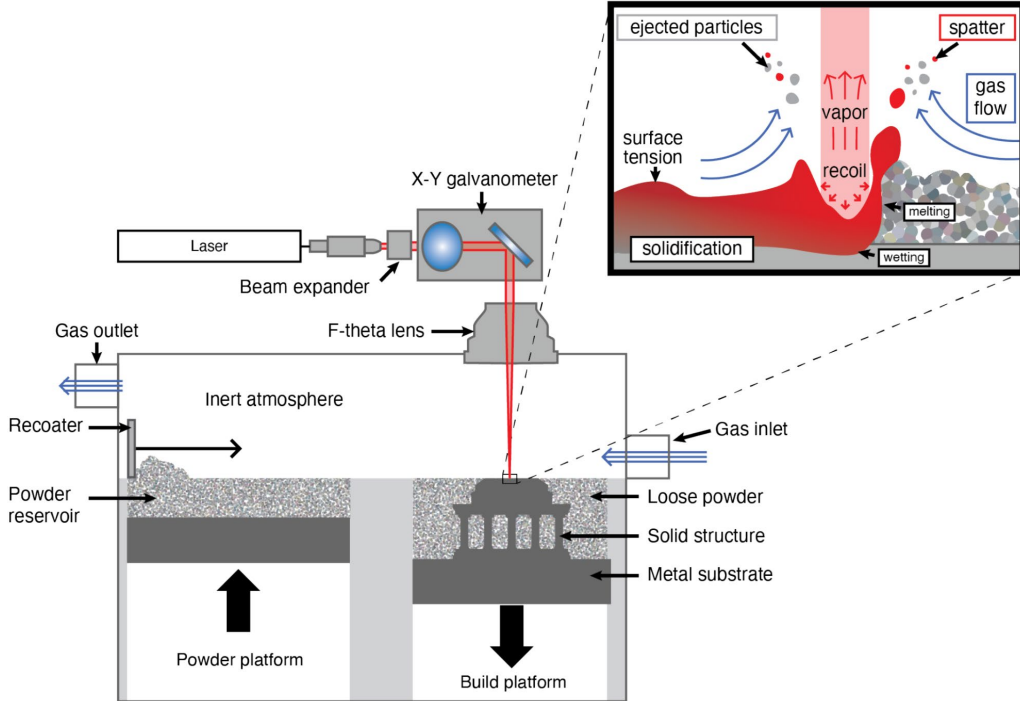


Figure 1. Overview of a typical SLM system and process. Note that the inert gas flowing over the built part helps carry away spatter and plumes of material. Adapted from [14].

The component is built directly off a plate driven by a piston to achieve the incremental layer heights. Powder is measured out from another piston or hopper and is spread across the build using a recoater, which is usually a blade or roller. This all takes place in an inert environment to ensure the material does not become oxidized during printing. Typically, more inert gas is flowed over the build region in order to carry away spatter and plumes of vaporized material from the build. These plumes would otherwise attenuate incoming laser radiation and may cause porosities/defects in the part [14]–[16].

1.2. Compositional Gradients and Functionally Graded Materials

Multi-material printing of functionally graded parts is a prime application of various AM processes that would allow designers to custom tailor a part's microstructure and/or material composition to yield specific properties. Such parts are said to be examples of functionally graded materials (FGMs) and are a very active area of manufacturing research [17]–[22]. Graded materials/components are actively explored and utilized in a diverse array of industries and products including biomedical devices, sensors and thermoelectric generators, and gas turbine blades [23]–[25].

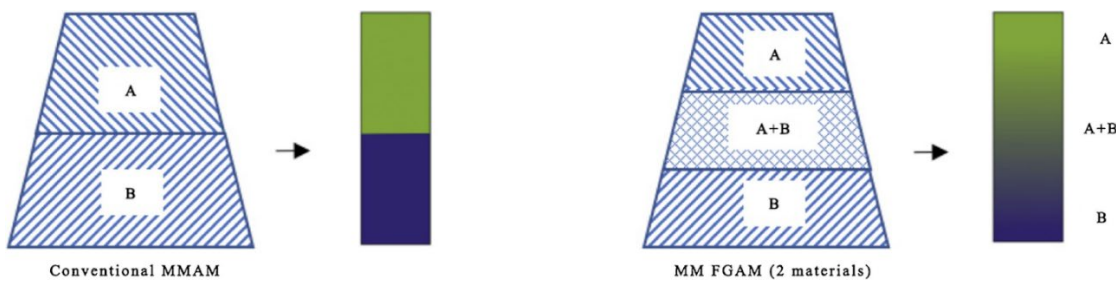


Figure 2. A sharp conventional gradient versus a smoother transitional gradient.

Most traditional coating processes still face issues of instability from thermal expansion, layer interdiffusion, and overall poor substrate adhesion resulting in delamination, cracking, and residual/induced stresses of the coating [26]. Compositional gradients may be used to incorporate a highly corrosion resistant alloy or ceramic directly into the skin of a part, which has the potential to remedy the stability issues present in traditional coatings [19]. A corrosion resistant skin also has the potential to be self-healing given that its depth, stability, and robustness may be greater than a traditional coating. Alternatively, the material properties of components could be varied spatially with the material composition and microstructure.

Compositional gradients have been created along multiple axes with DED processes by varying the composition of the feedstock/powder being blown into the melt pool as demonstrated by Oropeza et al. [27] and Kelly et al. [28]. However, the DED process is fairly limited in terms of the dimensional precision and resolution achievable, given that the typical laser spot size (and thus resolution/feature size) in such a process is on the order of millimeters, and layer heights are usually in the range of 200-650 μm [29]. The desire for greater spatial resolution and precision leads to SLM processes, where laser spot sizes of 60-90 μm and layer heights anywhere from 30-100 μm are typical [29]. Perhaps the most elegant implementation of FGM creation in a SLM

process may be found in mixing powder feedstocks layer by layer to create a gradient along the build direction as shown by Demir et al. [30]. This work provides a new level of precision in producing parts with a compositional gradient, though is still limited in the sense that the gradient's direction is limited to the part's build direction. Systems have also been created to selectively deposit powders in certain regions on the build plate. The startup iro3d created a very rough process where metal powders and support material is selectively deposited into a crucible and then sintered [31]. Within PBF systems, the company Aerosint has created a set of hoppers and separate rollers/recoaters to selectively deposit material across a powder bed [32]; and Walker et al. [33] have demonstrated a hopper/vacuum setup to both deposit and then selectively clean up different powders from the build surface. Both of these systems allow for a high level of control of material deposition within a SLM platform along any axis, though can still only produce sharp transitions between materials as opposed to smoother gradients. BJAM was also considered as a solid candidate though would have necessitated further equipment/complexity given that printed parts would need to be sintered, and that the accompanying warpage/shrinkage would need to be accounted for (likely through some iterative process). There was also some uncertainty as to how well alloys would form during sintering, as well as how to selectively change the amount/location of deposited alloying material.

1.3. Key System Design Parameters

In order to preserve the dimensional accuracy and process controls offered by SLM, though still enable finely controlled compositional gradients within components, inkjet printing was identified as a suitable material deposition method. Inks loaded with nanoparticles (NPs) of some alloying element could be deposited in small enough increments to allow for very fine control over the overall material composition by adjusting the number of layers deposited [34], [35]. The system presented here is thus a custom built SLM machine with an inkjet nozzle/gantry situated above the powder bed.

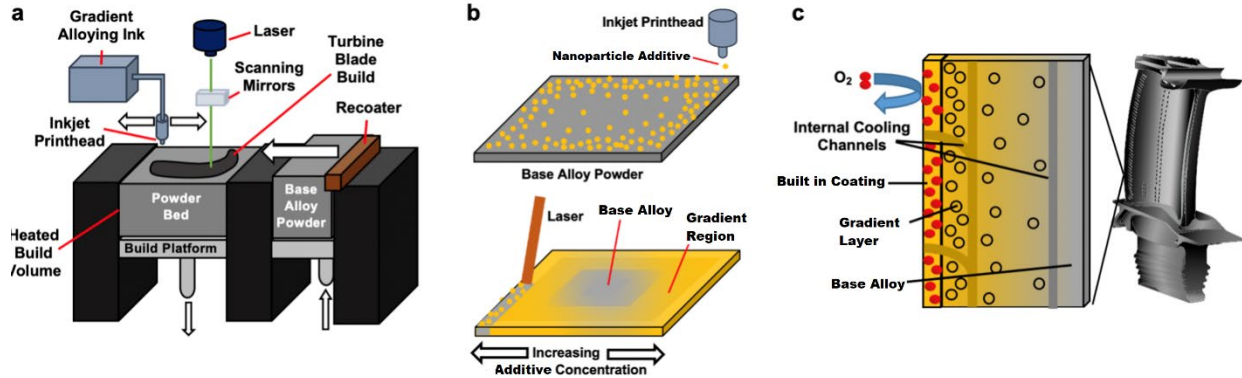


Figure 3. (a) The overall operation of the hybrid system, including layer-by-layer inkjet deposition; (b) layer-by-layer creation of the compositional gradient via inkjet; (c) possible application of a built-in oxygen resistant coating for additively manufactured

The inks typically consist of a filler and/or solvent (such as water or ethanol), the NPs of interest, and a dispersant to maintain the NPs in suspension [36]–[38]. The ratio of these ingredients is carefully adjusted to ensure that the NPs have a stable suspension, and that the ink's overall viscosity and surface tension will render it printable [39]. These additives generally vaporize either on contact with the bed (if it has been preheated) and/or upon laser scanning, and have not been seen to significantly impact print quality.

Drop-on-demand jetting was selected for this study given its simplicity and low entry cost as compared to continuous jetting systems. In some of these simpler and more robust inkjet nozzles, actuation is typically either from a resistive heating element (which flashes some of the ink into vapor) or a piezoelectric actuator [40], [41]. Even these simpler nozzles have still been shown to achieve material deposition with resolution on the order of 50-200 µm, spatial precision on the order of 10-20µm, and ink volume deposition on the order of 5-50pL [42], [43]. Research has been done by a number of groups investigating the use of metallic deposition via inkjet to produce simple circuits and circuit elements [38], [44] and even small metal structures [45]. There are also some studies focusing on laser curing of inks containing silver and gold nanoparticles [45]. However, at the time of writing there does not appear to be any effort towards creating a hybrid inkjet-LPBF process for in-situ production of metallic alloys.

Another important design consideration for the hybrid system presented here is preheating of the build volume. In an SLM process residual stresses accumulate as a part is built due to a combination of the highly localized energy input from the laser, rapid cooling rates, and resulting repeated material shrinkage and expansion [46]. These residual stresses may cause

failed prints, warped parts, and cracking throughout the part. Preheating the build volume significantly ($>300\text{-}400\text{C}$) has been shown to reduce the thermal gradients present as well as relax residual stresses as the part is built [47], [48]. Much of the future work conducted with this system is principally centered around creating parts from Niobium (Nb) and Nb alloys. Nb based alloys are a type of refractory alloy with an extremely high melting point (2477°C), lower density compared to other refractory metals (8.4 g/cm^3), and great high temperature strength and creep resistance [49], [50]. Because of this, they are of the most promising materials for energy and aerospace applications as an alternative to Inconel alloys as high temperature materials [51]. Production of Nb-based alloys is challenging via traditional casting and forging techniques, and so there is a growing interest in the production of Nb-based alloys via AM techniques [51]–[57]. However, one of the biggest challenges of refractory metals prepared through SLM or EBM is microcrack formation during solidification [58]. The high cooling rates and subsequent thermal gradients and residual stresses present in a typical SLM process is one of the principal factors in microcracking, along with oxygen embrittlement [59], [60]. One of the main strategies employed in previous studies for reducing microcracking in refractory allows is to preheat the build above the alloy's ductile to brittle transition temperature (DBTT). Previous work with Nb and other refractory alloys point to substrate temperatures of anywhere between $200\text{-}1100\text{C}$ to be sufficient to help eliminate DBTT type cracking [59], [61]–[64]. Based on previous work with refractory and stainless steel alloys, a maximum preheating temperature of 500C was chosen for the system presented here.

Instrumentation was also developed to investigate the feasibility of using a drop-on-demand inkjet setup on high temperature substrates. Inkjet nozzles are typically very sensitive to both environmental variables (i.e. humidity and ambient temperature) and fluid/process parameters (namely surface tension and viscosity) [41]. The nozzle orifice/substrate distance is normally kept relatively short (below 1mm for drop-on-demand systems) in order to ensure stable and accurate material deposition. Larger throw distances than this may lead to inaccurate deposition partly from the Couette flow resulting from the relative velocity of the printhead and substrate, other air/gas flows near the printhead, and mechanical perturbations from the printhead/nozzle [41]. Given the inkjet process sensitivity and orifice proximity to the substrate, printing on a high temperature surface may pose issues to the nozzle operation. Increases in temperature at the nozzle orifice may alter the viscosity and/or surface tension of the ink, forcing it out of its narrow operating regime.

Rapid material vaporization upon impact with the surface may also disrupt accurate jetting by providing unwanted thrust to droplets in flight.

The droplet/substrate interaction itself also warranted some attention. At elevated surface temperatures a vapor film begins to develop between the liquid-substrate interface, which may disrupt the quality of ink deposition. This is referred to as the Leidenfrost effect, and the critical temperature for its occurrence has not been effectively modelled at the time of writing. This transition point is very sensitive to the incoming fluid's properties, the droplet/stream properties (size, velocity, angle, etc), and the impact surface's thermal properties and physical features [65], [66]. For instance, experiments done by Burnardin & Mudawar with water on an aluminum plate show variations in this critical temperature from 170C to 280C while only varying the surface preparation/roughness of the plate [67]. Given the current state of Leidenfrost temperature modelling and the sensitivity of the inkjet process, a single-nozzle inkjet deposition apparatus was set up to empirically observe the droplet-substrate interaction at various temperatures on substrates relevant to SLM processes.

2. HAMR3 Design & Commissioning

2.1. Overview

The system described here is a custom SLM printer with an inkjet nozzle and gantry installed over the print bed to allow for higher flexibility in creating multidimensional compositional gradients on a layer by layer basis. The ink fed into the printhead is loaded with NPs of a desired alloying element up to 1-5 wt.%. The mechanical system (enclosure, powder manipulation elements, and inkjet gantry) take up approximately 800 x 700 x 900mm. The supporting electronics, gas controls, water chiller, and optical drive train take up the majority of a 4 x 1.5 x 2.5m space.

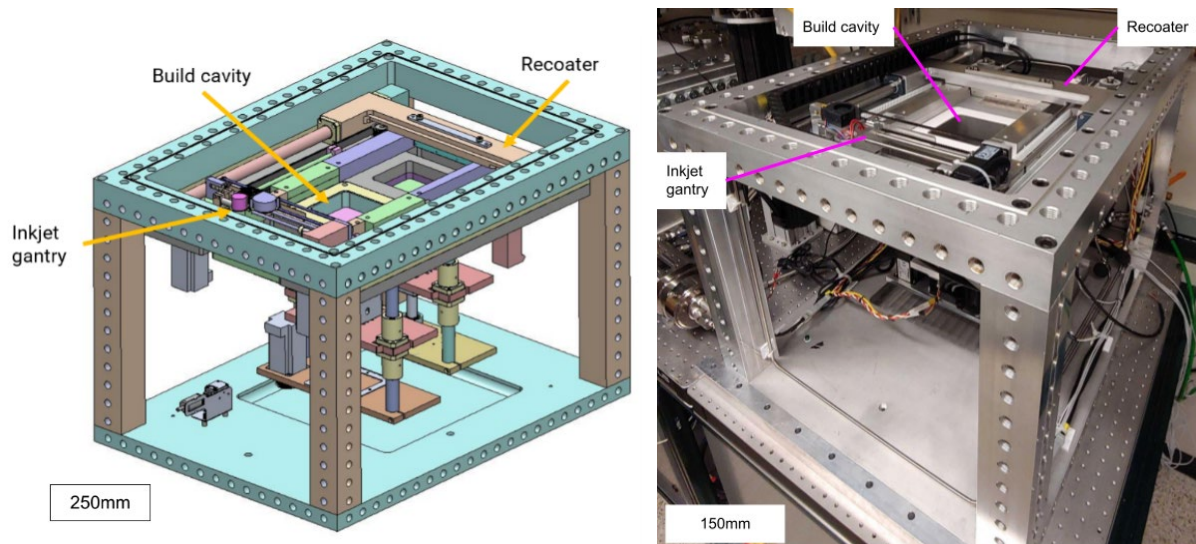


Figure 4. Overall views of HAMR3's solid model & actual construction without its enclosure.

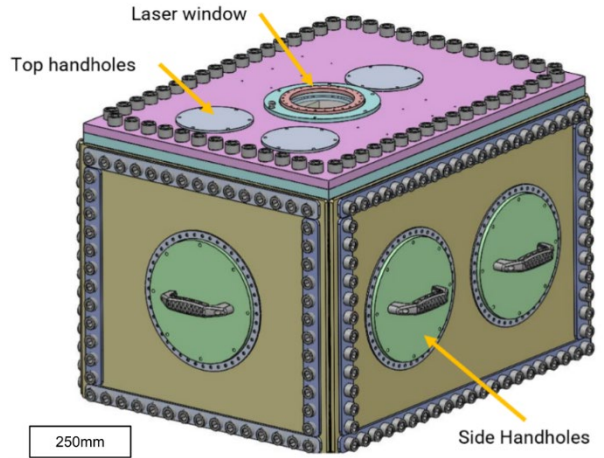


Figure 5. Views of HAMR3's outside enclosure including port holes and laser window.

The enclosure was made with numerous port/hand holes throughout the chamber so that nearly any part of the printer is accessible. The laser window itself may be removed to access the build platform/remove builds, and a port hole also lies over the supply piston to help simplify loading powder into the machine.

Table 1. HAMR3 specifications and capabilities

Parameter	Design Values
Spreader type	Interchangeable blade
Spreader traverse speed	5-1000 mm/s
Powder dispensing mechanism	Piston & inkjet nozzle
Inkjet nozzle orifice diameter	80 μ m (20-80 μ m available)
Build Temperature	20-500C
Build Volume	100 x 100 x 100 mm
Laser Power	50-550 W
Laser Wavelength	1064nm
Laser Spot Size	\geq 30 um (4 σ diameter, adjustable)
Laser Scan Speed	0 - 100m/s

The laser used (SPI redPower QUBE) outputs a continuous wave gaussian beam centered at 1064nm. A custom optical system is used to deliver the beam to the printer's chamber and is comprised of a collimator, turning mirror, galvanometers, and an f-theta scan lens. Further details of the optical system and its characterization may be found in a paper by Griggs et al.

[68]. To prepare the system's internal atmosphere for printing, the enclosure is first brought under vacuum until no further decrease in pressure is registered. Ultra high purity (UHP) argon is then used to fill the chamber. After filling, an exhaust port on the enclosure is opened and argon is allowed to flow/mix through the chamber at roughly 10-30 LPM until a downstream trace oxygen sensor (MTI EQ-W1000-Sensor-LD) registers an oxygen content of <300ppm (after about 60-90 minutes of flowing).

2.2. Build & Supply Pistons

The printer contains 2 pistons, one that controls the height of the built part with respect to the top plane of the printer (the build piston) and one that incrementally supplies powder to recoat the built part (the supply piston). The build and supply pistons both utilize servos equipped with 24-bit absolute encoders (Yaskawa SGM7J-02A7D61) to drive ball screws (custom from Misumi with a 1-3% preload) via a set of timing belts/pulleys. The servos and screws were chosen to gain a high level of precision from the movement of the pistons, such that the layer height for the built part would be very consistent and accurate. The ball screws are mounted in their respective base plates using a lightly preloaded back-to-back configuration of sealed angular contact bearings, making the assembly fairly rigid.

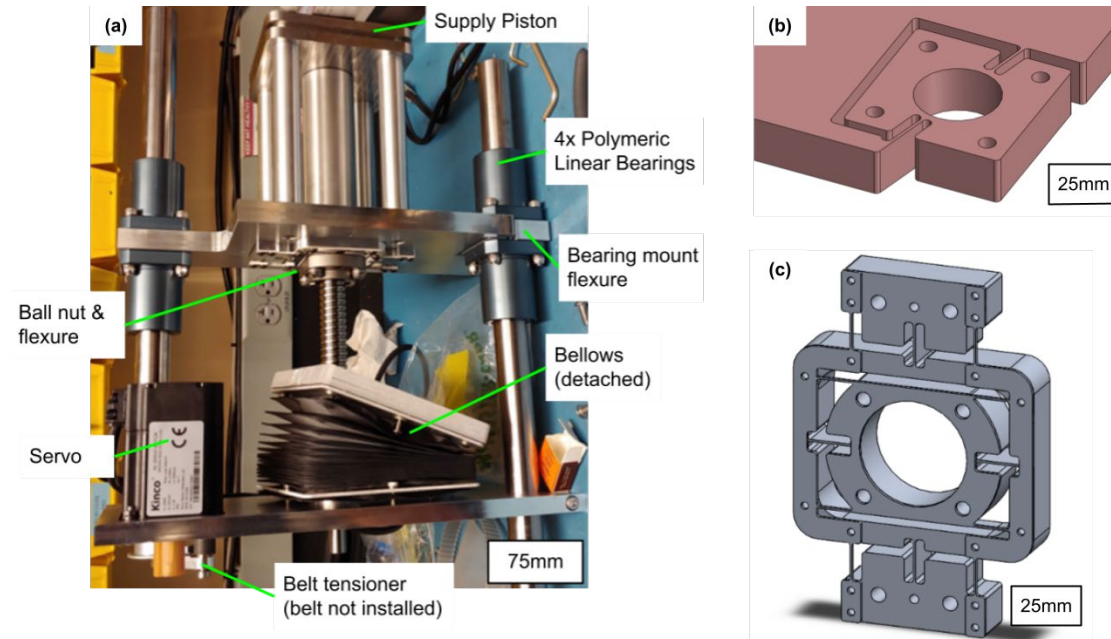


Figure 6. (a) Overall view of the supply piston, which is nearly identical to the build piston anatomically; (b) linear bearing mount flexure used on one of the guide rails; and (c) serial flexure used to mount the ball nut to the movement stage.

In order to avoid overconstraint the ball nut of the screw is attached to the moving stage/piston through a flexural element. The element in Figure 3(c) is a serial flexure designed to yield four degrees of freedom and/or to only rigidly constrain the ball screw along the build direction and about the rotational axis of the screw. Another flexure was employed in the second linear bearing mount (shown in Figure 3(b)) to allow for small angular errors with the guide rail that the piston's stage rides on. These flexures were included to mitigate linear position errors from overconstraint on each piston, once again to gain greater precision in the layer heights of the built part.

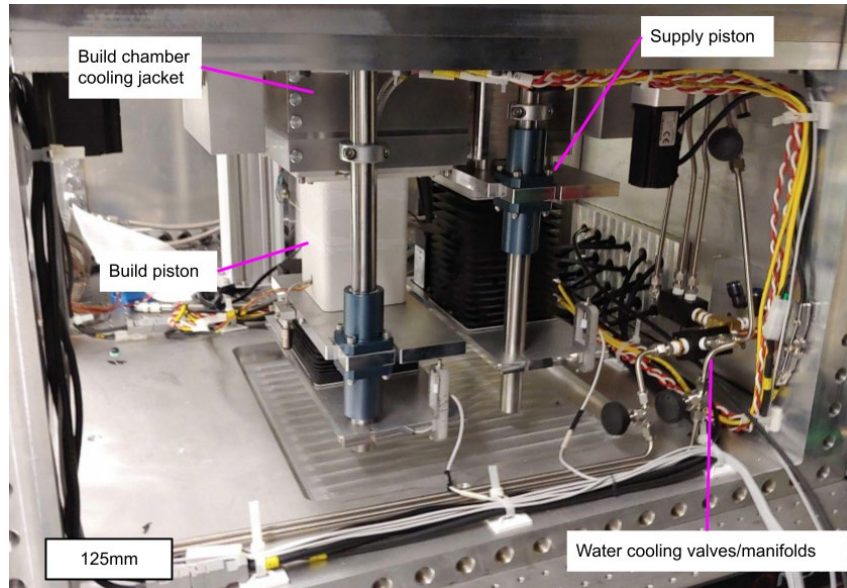


Figure 7. Side view of the printer without enclosure, where the installed build and supply pistons may be seen.

The stage of each piston is homed to a set of precision limit switches (Metrol CSJ055A-L), and the starting position offset may be found by directly measuring the height difference between the build/supply piston and the baseplate.

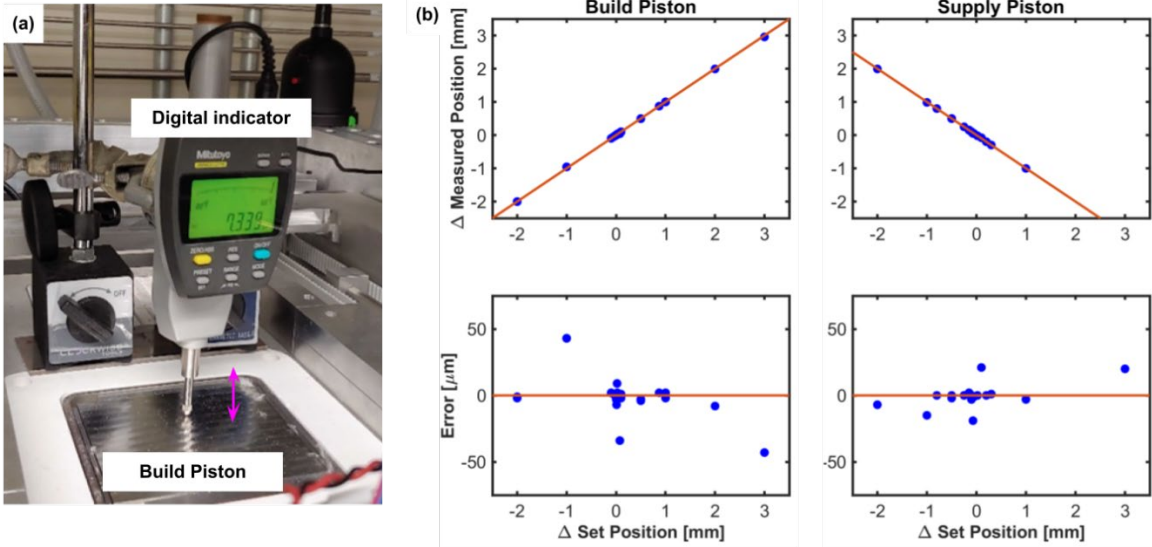


Figure 8. (a) Piston movement measurement setup; (b) change in set position versus measured change and overall error for the build & supply pistons.

A digital indicator was used to measure several incremental movements of each piston. Uncertainty analysis was used on the nominal and measured changes in piston heights to then determine the precision of the build and supply pistons, which turned out to be roughly 8 & 7 μm respectively. The handful of higher magnitude errors seen in Figure 8 are primarily attributed to hysteresis of the piston/its transmission, as they appeared to occur at direction reversal points. This is less of a concern for this machine since the pistons will not be reversing direction throughout the duration of the print.

2.3. Heated Build Volume

The system was made with fabrication of refractory metals and alloys in mind. These metals tend to have much higher melting and working temperatures than some typical metal AM materials, for instance the liquidus for Inconel 625 is roughly 1,350C [69] as opposed to pure Nb's melting point of 2,468C [49]. To reduce the thermal gradients in the part and energy input required, the build chamber of the machine presented here was designed to heat the entire powder bed and part up to between 500-600C while maintaining a maximum steady state thermal gradient of 100C throughout the build.

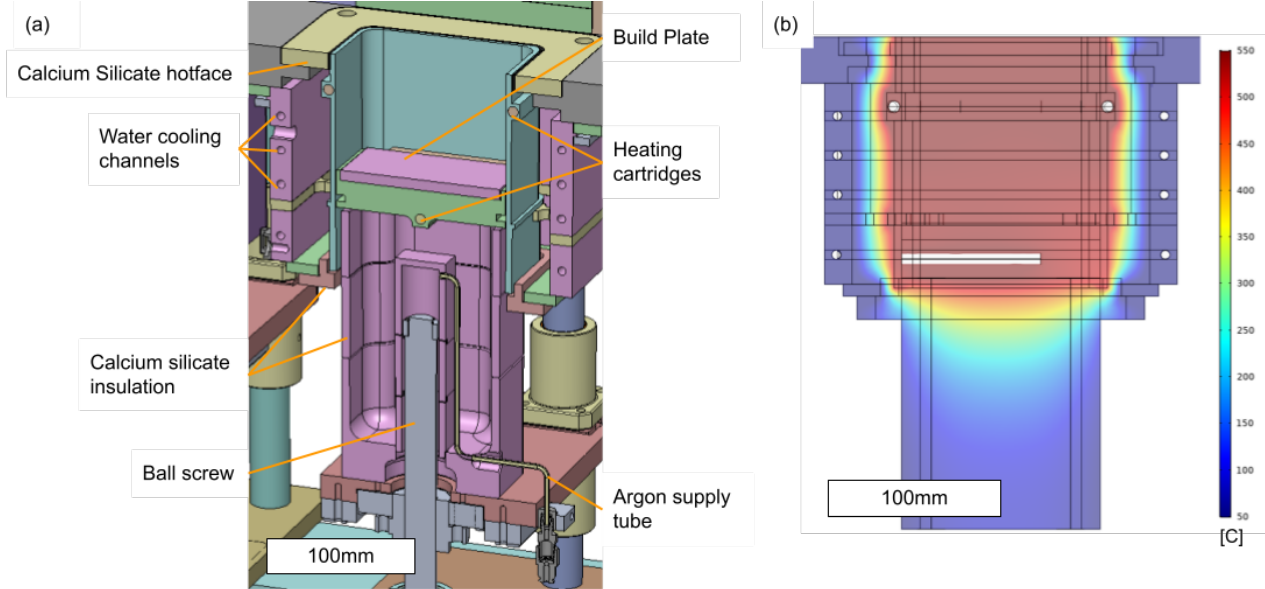


Figure 9. (a) Shows a cross section of the heated build volume and build piston along with the position of some of the resistive heating cartridges. The voids between the build volume and water-cooling channels as well as in the piston/screw insulation section a

The heated bed consists of a 405 series stainless steel liner and build piston. Build plates are machined with a chamfer on the top surface of both ends, and a mating chamfered plate is screwed into the piston to clamp down the build plate. Four 225W cartridge heaters and thermocouples (McMaster-Carr 8440T136) are integrated into the walls of the liner and an additional 175W cartridge and thermocouple (McMaster 8440T112) is in the build piston. A simple proportional-integral (PI) loop is used for each individual heater to ensure they maintain roughly the correct commanded temperature. Resistive heaters were chosen for their simplicity and cost effectiveness, though induction heating was also investigated and may be seen artfully integrated into Caprio et al.’s custom printer, *Grisú* [70].

In order to minimize the impact of the build volume’s heating on the rest of the assembly, the inner liner is wrapped in a ceramic fiber blanket (Kaowool). The inner liner is also suspended in the middle of the heater subassembly via a skirt (shown in Figure 8(a)) so as to minimize the amount of conduction from the liner to the outer shell of the subassembly. The aluminum outer shell has a network of holes drilled around its perimeter to allow for water cooling as well. The pieces capping the top and bottom of the subassembly are made from calcium silicate, chosen for its low thermal conductivity (0.3 W/mK) and high working temperature (up to 1000C). Additionally, a small diaphragm pump is used to pump argon in the chamber into the build piston’s screw cavity to maintain a screw temperature of below 50C .

2.4. Gas Knife

A stream of argon flows over the build surface while the laser is firing such that any plumes and spatters are carried away. This helps keep the optical path from the laser to the bed clear and allows consistent energy deposition to the bed, increasing build quality [15], [16]. To accomplish this flow (which will hence be referred to as a gas knife), a set of nozzles are positioned at either side of the bed. The nozzles themselves are simply a thin slit fed by a larger reservoir into which argon is fed.

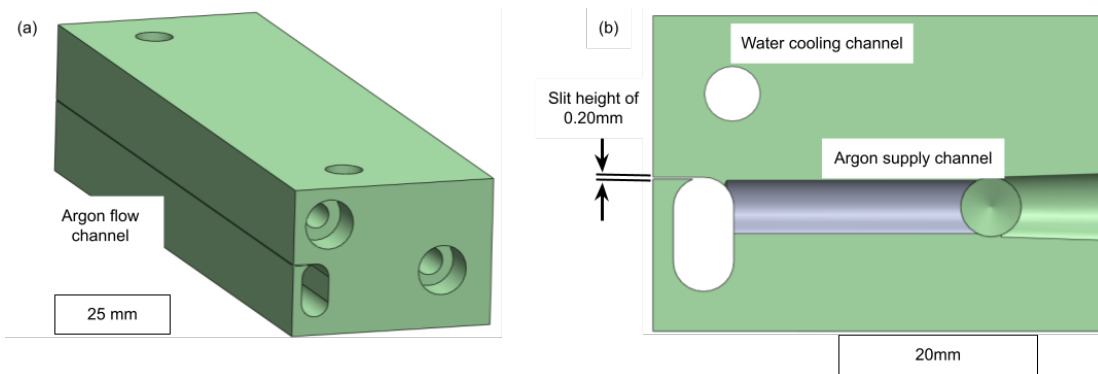


Figure 10. (a) Shows one of the nozzles and the porting on the end for water cooling and the argon supply. The second argon reservoir is open at the ends for ease of manufacturing, though the mating channels help to seal this. (b) shows a cross section of the nozzle.

Since the build surface is to be maintained at a bulk temperature of 500-600C, the argon returning from the gas knife as well as the flow nozzle requires cooling. Thus, a water cooling channel is run alongside the gas return channel for the length of the build platform. The nozzles and side walls of the build surface are also in good proximity to the heated build volume, and so the water cooling here also serves to regulate the temperature of the baseplate.

The flow rate through the nozzle should be maximized such that it swiftly carries away the greatest amount of spatter, but hits a limit of powder disruption. This critical velocity is dependent on numerous factors to include the powder size, shape, density, etc. Based on work done by Kalman et al. [14], an initial estimate of 1-2 m/s was assumed for the critical velocity of the system's powder bed. From this estimate a set of flow controllers, valves, and filters were assembled and used to control the gas knife.

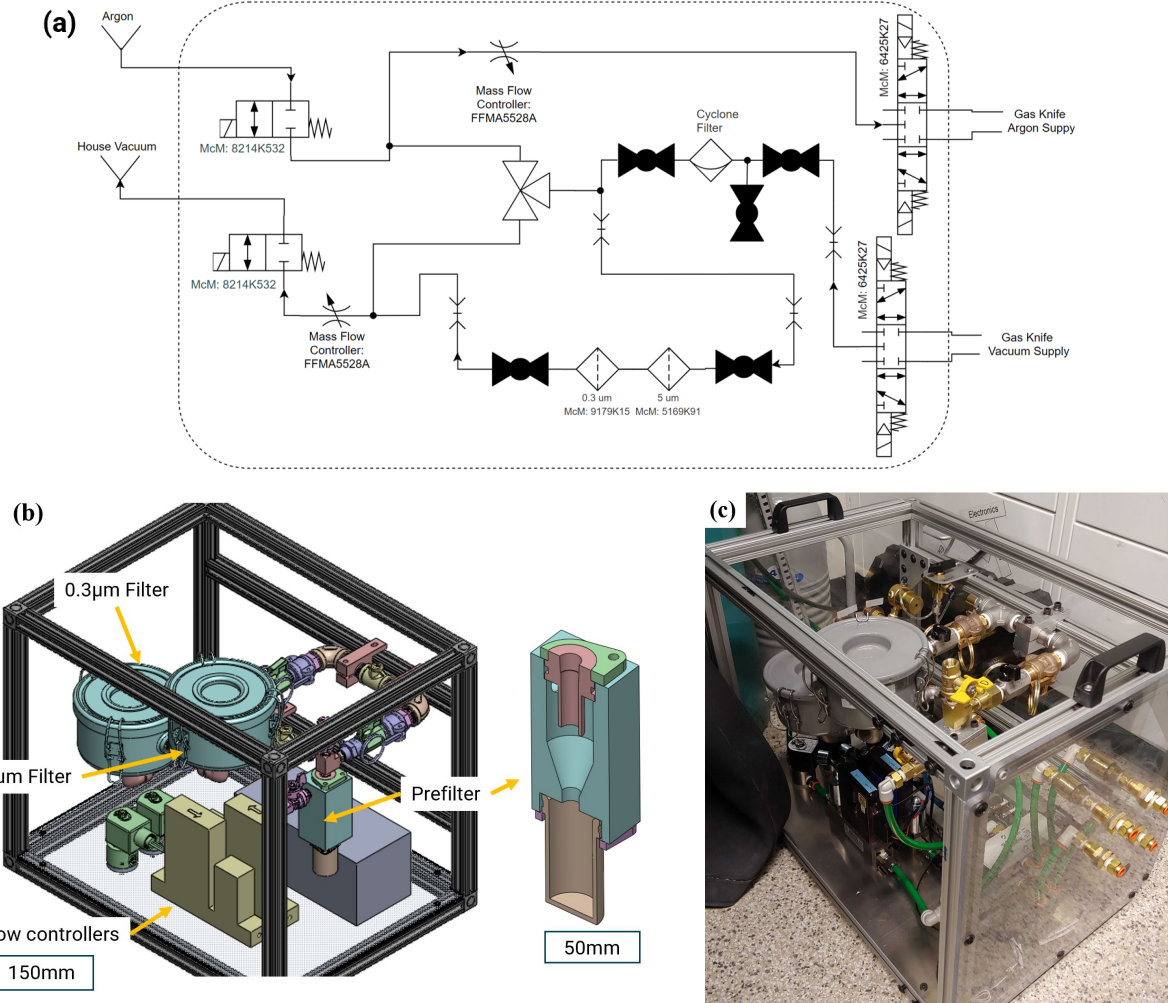


Figure 11. (a) Schematic of the gas knife control and filter setup; (b) solid model of the controller/filter assembly, with a cross section showing the internals of the cyclonic prefilter element (with the collection bin on bottom and the outlet shown at the top).

The exhaust fumes extracted by the gas knife also contain powder/material ejected from the print bed. This material varies from larger clumps of material (likely 15-200 μm) from partially fused powder down to very fine powders (0.5-1 μm) from spatter and vaporized powder, and may become unpassivated and/or highly reactive to oxygen/air during its formation in the enclosure. A three-stage filter was devised to handle removal of these materials before they could cause damage to the mass flow controller used on the gas knife or the facility's fume exhaust and vacuum system. The first stage consists of a custom cyclonic filter designed to capture particles greater than 15 μm using design tools from PowderProcess [71]. Preliminary tests on this filter with 15-45 μm powder showed greater than 90% efficiency at the flow rates/pressures expected during printing use.

The second and third stage filters are off the shelf vacuum rated air intake filters rated at 99% efficiency for particles down to $10\mu\text{m}$ and $0.3\mu\text{m}$ respectively. The overall system has additional valving and disconnects to allow a user to isolate and remove each set of filters while they are under argon, perform a wet passivation on the filter elements, and then vacuum/purge the elements with argon before reinstalling them. Filter health is determined by whether the flow rates from each set of mass flow controllers (one supplying argon and one controlling extraction) are matching closely enough. Additional sensors and electronics are used to ensure that the gas knife will only operate once the enclosure's oxygen content is low enough such that oxygen/air will not be pulled into the extraction line/filters.

The critical velocity of the powder was then found experimentally by varying the controller's set flow rates and observing whether a layer of powder was disturbed by the gas knife.

2.5. Inkjet Gantry

The inkjet subassembly consists of a printhead/nozzle guided along an XY gantry. The gantry is driven by a pair of servos equipped with 2,500PPR encoders (Kinco KNC-SRV-SMH40S-0005-30AAK-4DK), one for Y positioning and one for X positioning. Initially the gantry was designed such that two servos would synchronously drive X axis, though this was altered since reliable synchronous position control of the axis proved difficult. The X axis is thus only driven on one end and rests/glides on top of the opposing rail, utilizing a piece of PTFE to minimize friction between the surfaces. Both axes utilize a pair of rails and linear bearings for motion; the mounting for the Y-axis pair of rails includes one rigid clamp and one flexural clamp so as to not overconstrain the gantry's motion. Once again, the choice of servos and flexures here is based on the spatial precision required of the inkjet and/or deposition of alloying elements. The linear bearings chosen (Igus Drylin series) use a polymer lining and are meant to run dry, yielding exceptional resistance to dust and dirt from their operational environment. This is important since they will be in close proximity to metal powders.

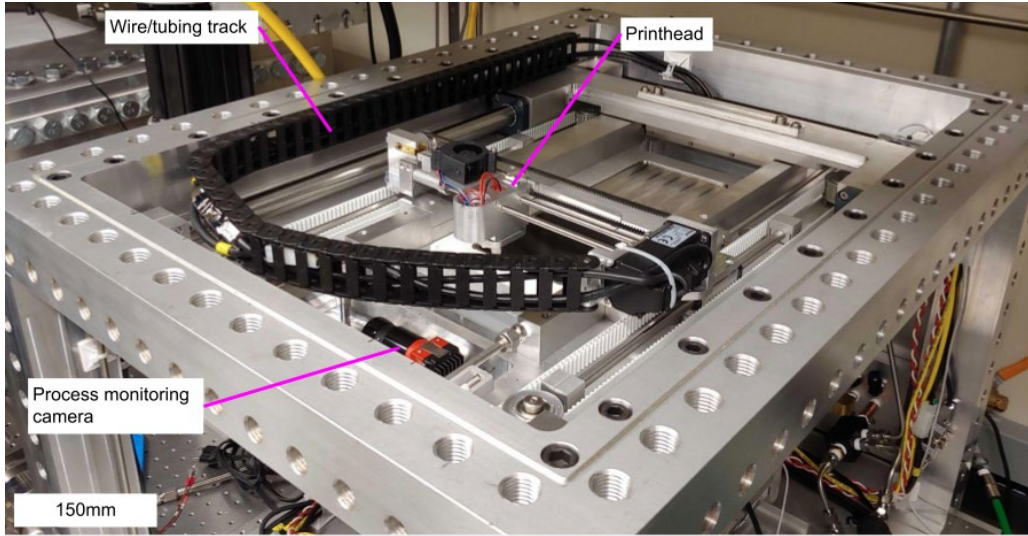


Figure 12. Top view of the printer without enclosure with the inkjet gantry/printhead visible over the empty build chamber.

A single nozzle (MicroFab MJ-AT-01 series) with an 80 μm orifice was used within the printhead, though nozzles with orifices down to 20 μm are commonly available and relatively simple to swap in. In order to function reliably the ink within the nozzle and at its orifice needs to be kept within a certain temperature range so that its surface tension and viscosity remain within a very narrow operating regime [41]. The pressure applied to the ink reservoir also needs to be kept roughly constant to ensure steady jetting, and is typically less than 0.20 PSI greater than the environment's pressure. Deposition is further complicated by the desire to preheat the build substrate to 500-600C; to achieve any level of spatial precision or accuracy with the inkjet deposition, the nozzle orifice needs to be kept roughly 1mm from the jetting surface. In order to get the nozzle close enough to the build surface while maintaining its orifice/body temperature, a thin plate of polished stainless steel (with another orifice) and an air gap was used to provide a layer of thermal insulation. The printhead also has a thermoelectric cooler on top and an RTD near the nozzle tip to allow for some degree of control over the bulk temperature of the nozzle.

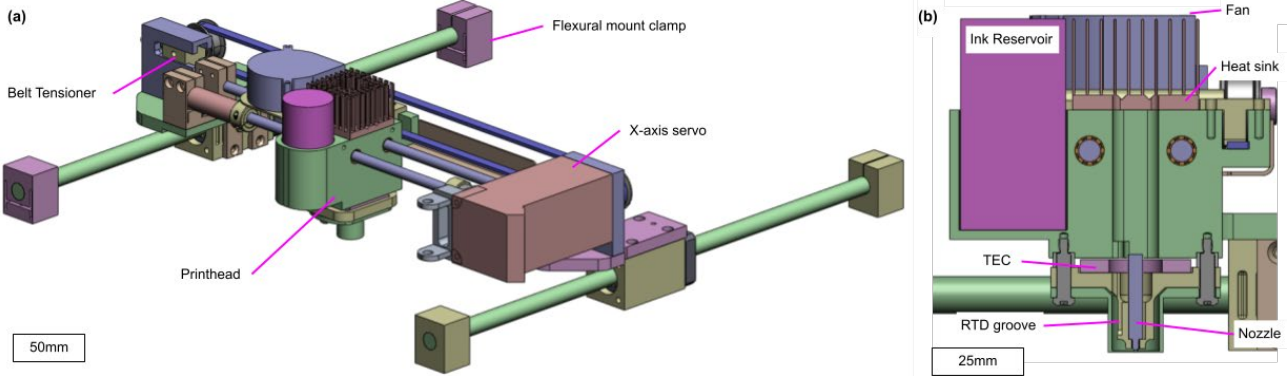


Figure 13. (a) Shows a solid model of the inkjet gantry assembly (aside from the motors, belts, and pulleys that move the y-axis), and (b) shows a cross section of the printhead.

The primary ink reservoir is a 30mL vial stored on the printhead. The pressure differential required of the reservoir/nozzle is small enough that jetting may be interrupted by the rate of change of the tubing's bend radii and/or by certain motions of the line itself. Keeping the feedline from the reservoir as short as possible and within the same inertial frame as the nozzle was done in the hopes of mitigating these sources of line pressure variation. A differential pressure controller (Alicat PC-1PSID-D/5P) was used to control the upstream pressure applied to the inkjet reservoir.

Ink development and characterization was done in large part by Emre Teko\u0111lu. The ink is a mixture of a polymeric deflocculant/dispersant (BYK DISPERBYK-2018), water, ethanol, and typically 1-5 wt.% of a NP of choice. The NP weight fraction simply depends on how much alloying element is desired per drop and/or the requirements on the generated gradient, though beyond 5 wt.% the nozzle tends to clog much more readily and the stability of the suspension of NPs degrades. The exact weight fractions of the components of the ink are presented in greater depth in Section 3.1 of this paper. Chapter 3 as a whole also takes a closer look at the interaction of the formulated inks with a heated substrate.

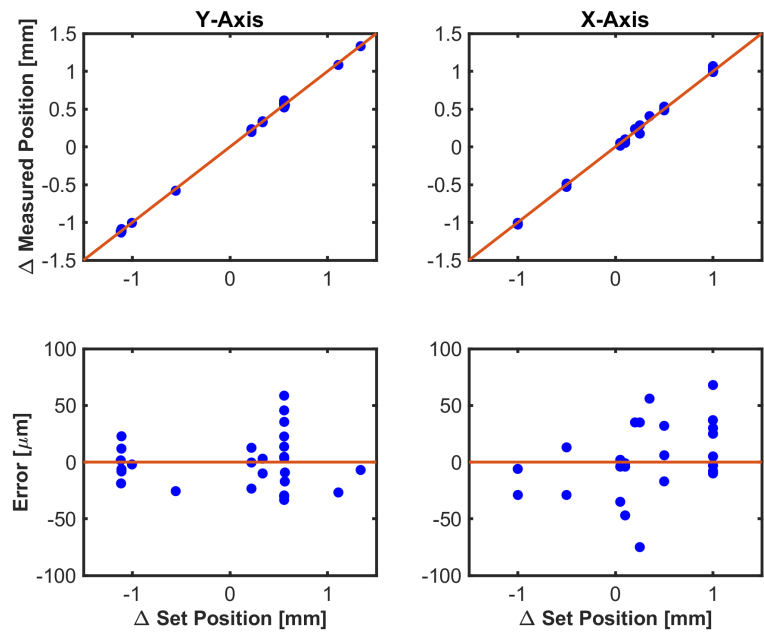


Figure 14. Printhead movement precision and error charts

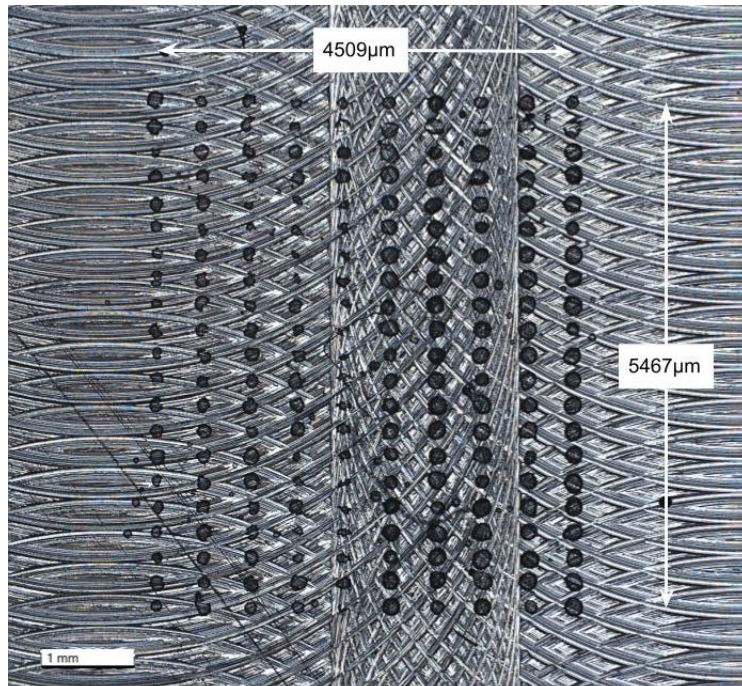


Figure 15. Example grid of dots jetted on a stainless steel plate.

2.6. Recoater

In order to take powder dispensed from the supply piston and uniformly coat the built part, a stainless steel blade with a 30 degree tip angle is swept back and forth along the top plane of the printer. The sub-assembly comprising this blade and providing for its movement across the supply and build pistons is referred to as the recoater. The recoater was designed such that the blade is easy to access and exchange for other profiles. The blade is mounted such that its height from the build surface can be gauged and adjusted with the top set of mount screws. The body of the recoater is translated over the build plate via two synchronously driven servo motors (Yaskawa SGM7J-02A7D6). The precision of the servos is less critical here though helps assure that the recoater is sweeping powder across the build piston at the correct speed (which may influence the quality of the powder layer that is deposited).

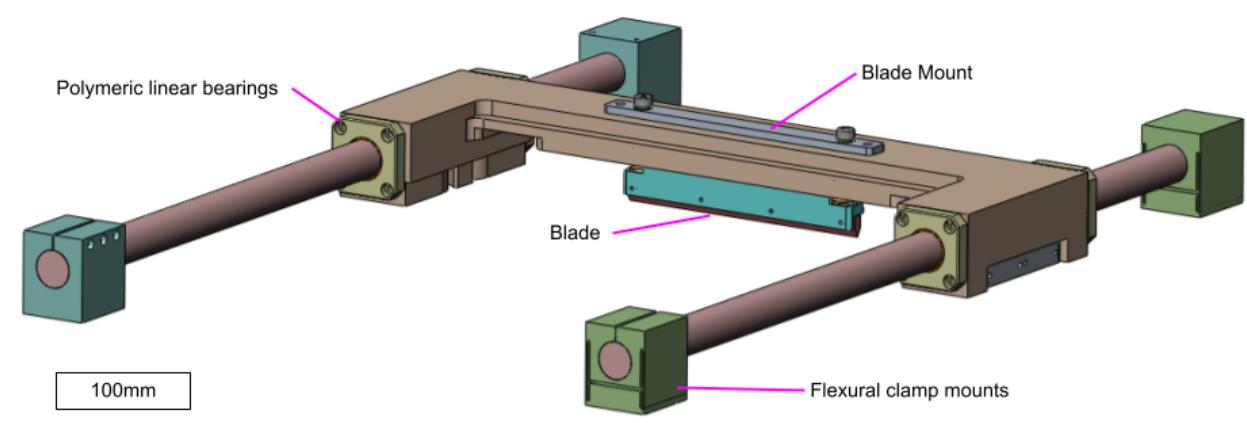


Figure 16. Solid model of the recoater subassembly (pulleys, belts, and drive motors not included).

A pair of rails and dry running polymeric linear bearings (Igus Drylin series) were used for guiding the motion of the recoater. To avoid overconstraint one pair of rod mounts are double blade flexures. Only one mount of each pair actually clamps down on the linear rod, while the other is a close slip fit to allow for differences in length that may evolve while the machine's temperature varies.

2.7. Control Electronics & Software

The entire system is controlled and coordinated by a LabVIEW program custom developed by Eagle Lake Systems. The servos that drive the build piston, supply piston, and the inkjet X axis are ran in position control mode. That is, these servos simply move to a commanded position and stop once they are there. The recoater and inkjet Y axis servos are ran in velocity control mode. This allows the inkjet to move to a desired X coordinate and then sweep a line in the Y axis at a given velocity, which along with the jetting frequency determines the droplet spacing. A desired inkjet pattern is created by positioning the gantry in X, running it along a constant velocity in Y, and then triggering the nozzle (via the Microfab JetDrive) when it is in the correct location(s). The desired jetting frequency, voltage, and ink pressure is set only once at the start of the print to the JetDrive and pressure controller.

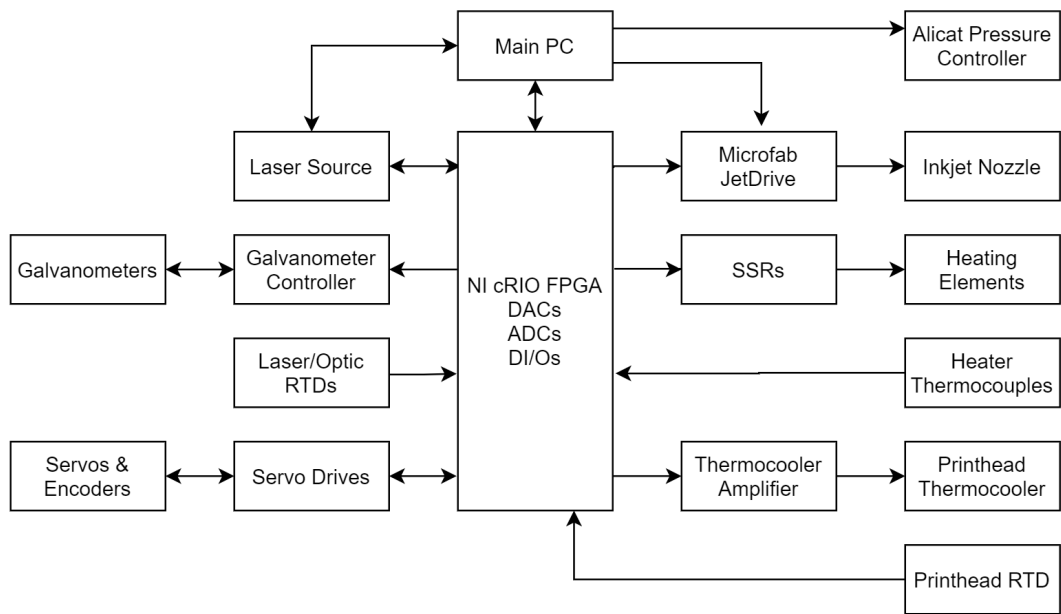


Figure 17. Schematic of system wide electrical controls. The heart of the system is based on a custom LabVIEW code base ran on a National Instruments cRIO FPGA with an array of DACs, ADCs, DI/Os, and other modules attached.

The laser scan is done by simultaneously sending the galvanometer controller and laser source a stream of position/power commands discretized into $10\mu\text{s}$ segments. Several temperature sensors are positioned around different optical components to help monitor for failure and subsequent thermal runaway of the lenses and mirrors.

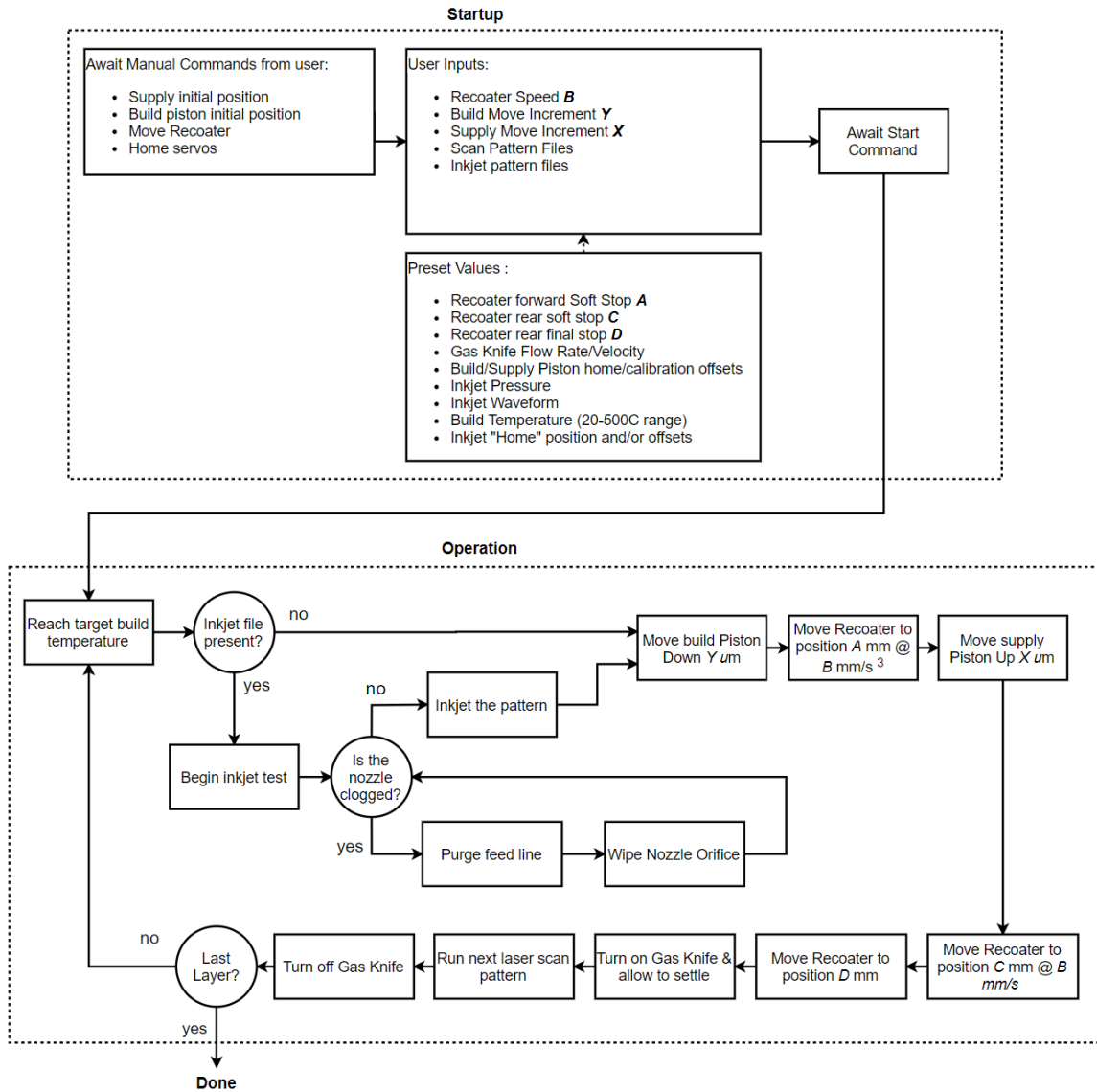


Figure 18. Sequence of events for a typical multilayer print in the system. The machine user may need to assess the nozzle function and make adjustments to its supply pressure and/or wipe the nozzle between layers.

3. High Temperature Inkjet Testbed

As mentioned in the discussion of the key design parameters for the overall system, inkjet deposition onto a high temperature surfaces poses a number of challenges owing to the complicated physics behind the inkjet process. The possible instability in the droplet's trajectory upon coming near/impacting a heated substrate (namely due to the Leidenfrost effect) also challenges accurate material deposition. In order to further characterize the drop-substrate interaction and deposition stability in such an environment, an apparatus was built to study the effect of substrate temperature on the inkjet process.

3.1. Apparatus & Experiment Overview

A custom testbed was assembled to allow for consistent jetting onto a high temperature surface. The testbed was built around a MicroFab inkjet nozzle and consists of an inkjet driver (MicroFab JetDrive V, CT-M5-01) and a precision pressure regulator (MicroFab CT-PT-21). Future work on this apparatus may require an environment with low levels of oxygen, and so the printhead and substrate platform was placed inside of an enclosure. An argon flowmeter was installed into the enclosure, and the sides of the enclosure may be sealed with additional panels so that argon may fully flood the space. The enclosure has the added benefit of limiting stray currents/flows in the room's air from affecting the inkjet process.

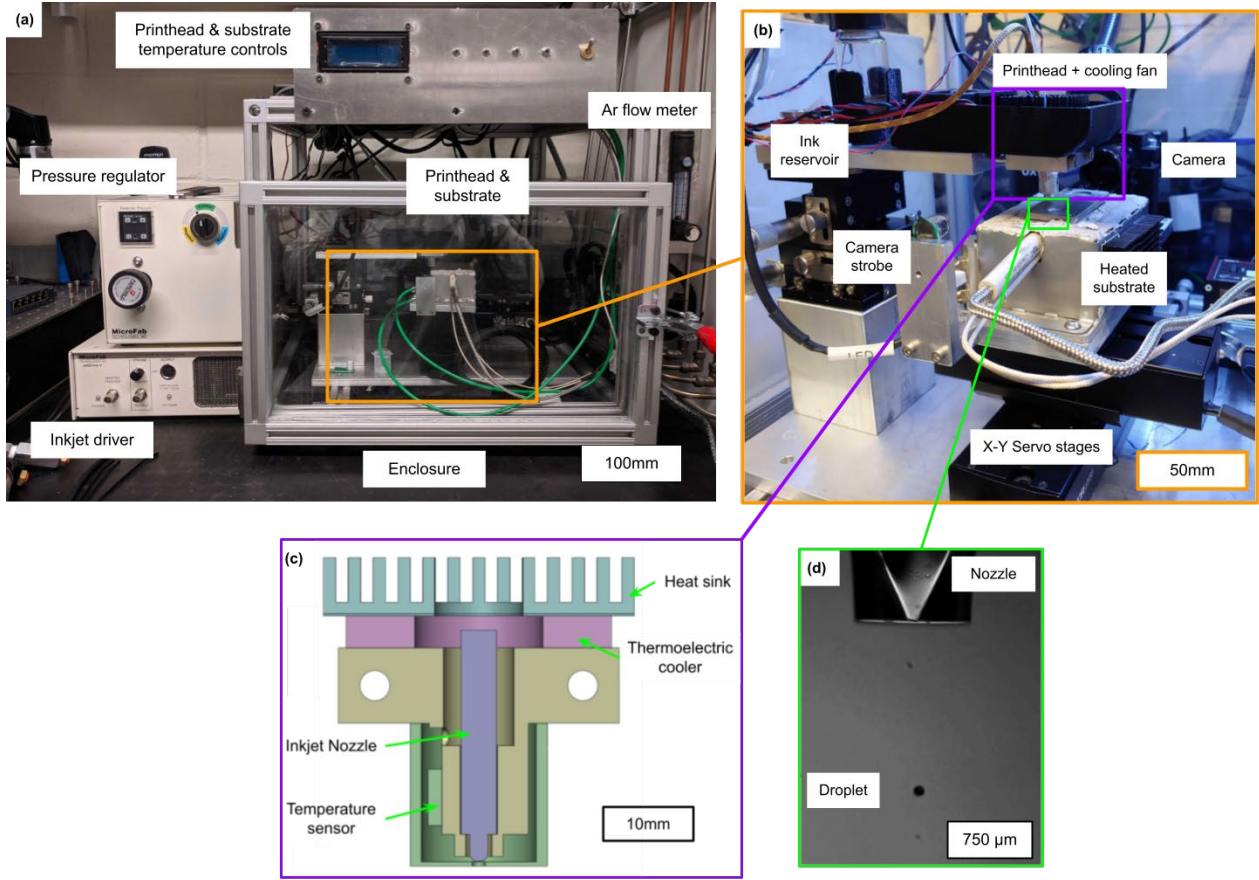


Figure 19. (a) Overall inkjet system with MicroFab pressure regulator and nozzle driver, enclosure gas controls, and substrate/printhead temperature controllers. (b) Printhead, substrate heater, substrate servos, and process camera assembly; (c) cross-section of printhead; (d) individual droplet getting dispensed.

The inkjet testbed, shown in Figure 1(c), has an inkjet nozzle with an 80 μm orifice diameter (MicroFab MJ-AT-01-080). This orifice size was the largest easily available, which helped to reduce the risk and rate of clogs. Jetting was performed using a custom LabView program to control the jetting locations, nozzle traverse speed, and the waveform sent to the inkjet nozzle. The substrate position and velocity were controlled with the use of two precision servo stages (ThorLabs DDSM50). Si NP inks were deposited across 316 Stainless Steel substrates. Figure 1(d) shows a formed droplet after stabilization of the process captured by a process camera and strobe (CM-VSU-03-90 and a pulsed LED).

Jetting was performed at several different substrate temperatures to understand how much preheating the inkjet process could endure. In an attempt to ensure consistent jetting regardless of substrate/environmental temperature, a thermoelectric cooler was employed within a custom

print head to precisely maintain the inkjet nozzle and ink at 20C (Figure 1(c)). A thermocouple was potted with high temperature/high thermal conductivity epoxy in a groove machined in the side of the printhead such that it was very close to the tip of the printhead, allowing for closed loop control of the printhead temperature. Originally a stainless steel outer shell (shown in green in Figure 1(c)) was machined to provide further thermal insulation to the nozzle's tip, though this made it difficult to monitor the jetting process. This shell was ultimately deemed unnecessary given that reliable jetting was achieved at substrate temperatures over 300C without it. The substrate was heated and held at certain temperatures with the use of a resistive heating element with an integrated thermocouple. Both the printhead and substrate temperature control were accomplished with simple PI control loops.

Table 2 shows the ink formulation utilized in this study. Work by Abbott [72] mentions inks used in an inkjet being confined to viscosities of 8-20cP and surface tensions of 25-50 dyne/cm. A polymeric wetting/dispersing additive (DISPERBYK-2018, BYK Company) was used to both bring the ink viscosity within printing range as well as help maintain Si NPs (SkySpring NanoMaterials, 99.7% purity, particle size \leq 500 nm) in suspension. Deionized (DI) water and ethanol were used in a 4:1 ratio as demonstrated in Oropeza et al. [42] in order to obtain a surface tension within the mentioned range as well as provide a solvent for an added polymer. Inks were prepared in a glove box under 99.999% purity argon (Linde, Marlborough, MA, USA) to prevent oxidation of the nanoparticles before mixing them with the liquid media. Strip ink patterns were jetted with 1 mm width and 12 mm length. The volume of a single layer of ink with the spatial dimensions 1 mm x 12 mm printed on an individual well surface is approximately 0.001mL. Jetting was also performed on a bed of Nb powder (American Elements, 99.9% purity, 15-45 μ m diameter particles) at different temperatures.

Table 2. Nanoparticle ink formulation utilized in this study (by wt%)

Deionized water	Ethanol	DISPERBYK-2018	Si NPs
77.6	19.4	1.0	2.0

To help better visualize the interaction between the substrate and inks, a high-speed camera (Phantom Vision Research) equipped with a microscope objective was aimed to capture the nozzle tip and substrate during jetting. The distributions of the powders and jetted patterns were observed

by Emre Teko\u0111lu using a Zeiss Merlin high-resolution SEM (Carl Zeiss AG, Oberkochen, Germany), which is equipped with an energy dispersive spectrometer (EDX).

Table 3. Utilized inkjet parameters.

Jetting frequency (Hz)	100
Jetting speed (mm/s)	10
Droplet spacing (μm)	100
Jetting voltage (V)	60
Nozzle diameter (μm)	80
Number of printed layers per strip	40

3.2. Experimental Results

The ink formulation in Table 1 was used to test how variations in substrate temperature affect the inkjet process. Ink with Si nanoparticles was jetted onto a lightly polished stainless steel 316L substrate at different substrate temperatures. The strip ink pattern was clearly visible until 200C (Figure 4(a-c)). Once the substrate reached 250C, the strip ink pattern became much fainter (Figure 4(d)). Pushing the substrate to 300C resulted in the complete loss of the ink pattern (Figure 4(e)).

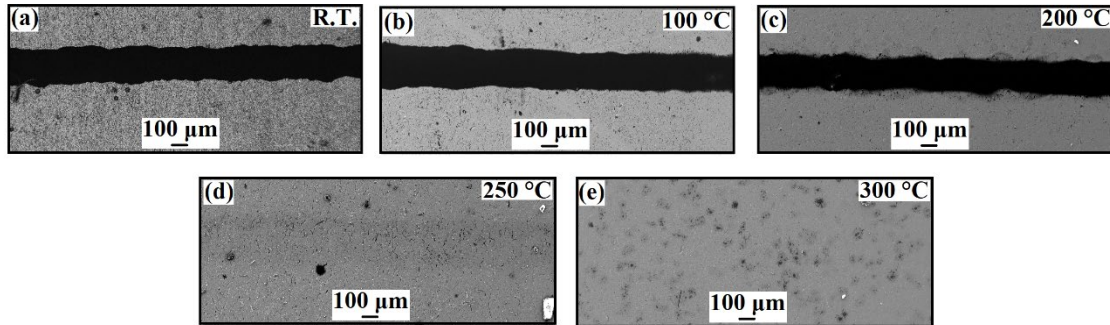


Figure 20. Jetting at various temperatures and the resulting SEM images showing the stability of the process. The line from (a) is roughly 47.5 μm , (b) is roughly 52.5 μm , and (c) is roughly 50 μm .

Emre Teko\u0111lu performed SEM and EDX mapping which yields a rough measure of the quality of the ink deposition at various substrate temperatures. Jetting on a 200C substrate shows a relatively homogeneous distribution of Si and C compared to the ones jetted 250C and 300C substrates. The observed carbon comes from the residual DISPERBYK-2018, which is not expected to completely degrade at the studied substrate temperatures (Figure 5(a-c)). When the

substrate reached 250C the distribution of Si and C is not as stable as when it was 200C, though once again there is still a faint line (Figure 5(d-f)). When the substrate reached 300C and above the Si and C signals were scattered over the substrate with a complete loss of the intended line pattern (Figure 5(g-i)).

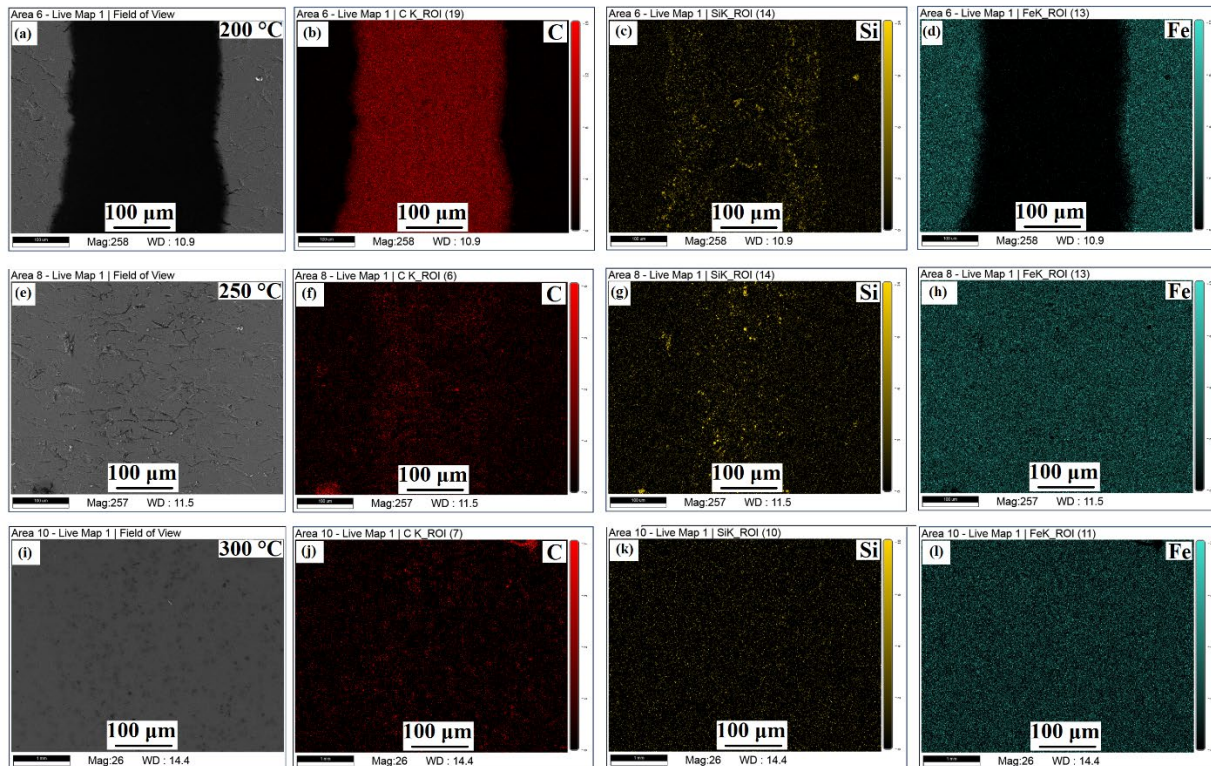


Figure 21. SEM images and EDX mappings of lines jetted under different temperatures. The line pattern once again becomes faint at roughly 250C and disappears at 300C.

A high-speed camera was used to observe the droplet-substrate interactions at various temperatures. Ink containing Si NPs was once again used, though this time the nozzle was stationary during the high-speed camera screening process in order to capture individual droplet movements. Figure 6 shows the trajectory of a droplet onto a 316SS plate held at 20C, 220C, and 250C. At 20C the drop (though faint in the images) appears to strike the plate directly where intended without bouncing or moving thereafter. At 200C incoming droplets appeared to often bounce and scatter after hitting the substrate. When the substrate temperature was 250C-300C the droplets tended to erratically bounce and/or scatter all over the substrate. It is apparent that the abrupt evaporation of water and ethanol forms a vapor film around the droplets and this introduces a thrust force when they approach the substrate.

This setup (ink with Si NPs, a high speed camera, and a stationary substrate) was also employed to observe the interaction between the ink and a Nb powder bed that was spread by hand using a razor blade into a well that was roughly 150 μ m deep. The powder bed temperature was varied between 20-320C. With substrate temperatures under roughly 250C the ink appeared to mostly wet and/or penetrate into powder bed. Above 250C the ink would at times appear to scatter across the bed upon impact. Additionally, above 250C droplets that appeared to wet/penetrate the bed would often rapidly vaporize after penetration, spraying small clumps of powder across the bed.

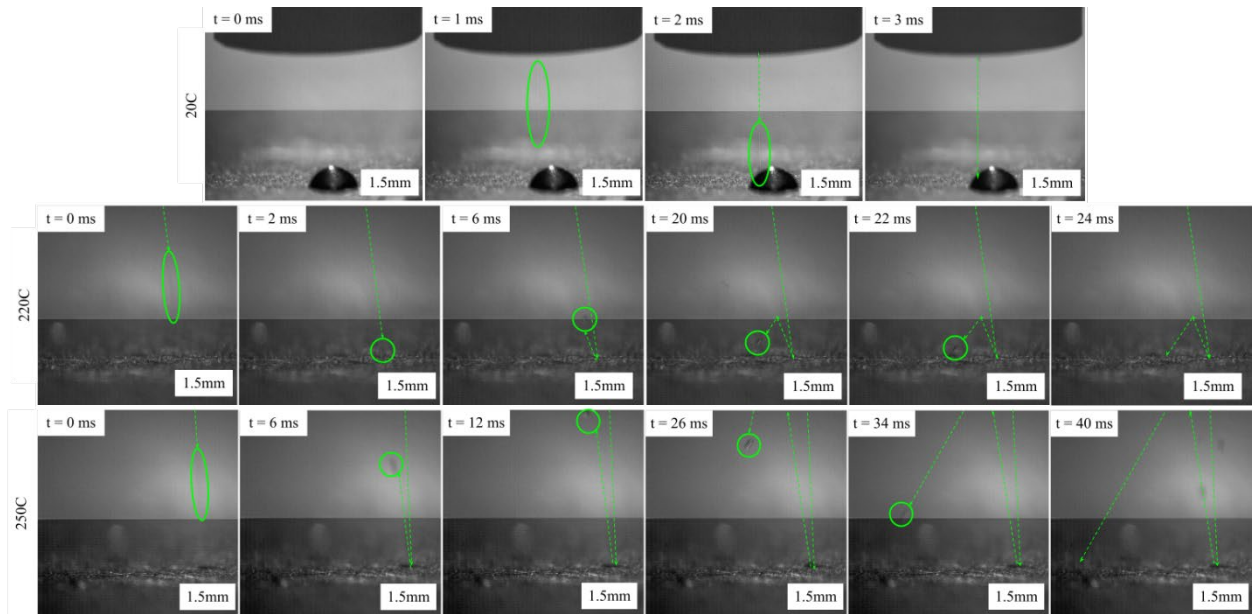


Figure 22. Inkjet droplet onto 316SS substrate at 20C, (top), 220C (middle), and 250C (bottom). The green dotted line shows the path of the droplet, and the ellipse/circles indicates the droplet itself. Note that the drop bounces around after impacting the substrate.

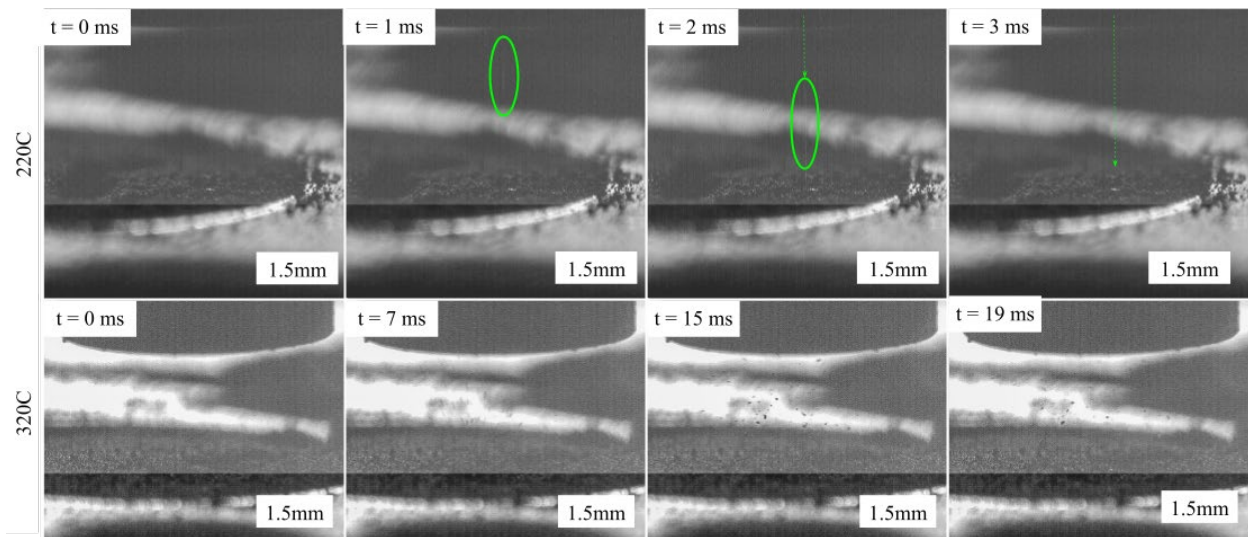


Figure 23. Ink droplet onto Nb powder at 220C (top) and post deposition interaction of ink and Nb powder held at 320C (bottom). Most droplets did not appear to bounce as on the 316SS plate but rather seemed to penetrate the bed and, upon vaporizing, sent powder flying

Emre Tekoḡlu also performed differential scanning calorimetry (DSC) and thermogravimetric (TG) analyses on inks with 10 wt% DISPERBYK-2018 and no Si NP to understand the behavior of the constituents in the ink as a function of temperature. Almost 90% of weight lost was seen between 0-100C, indicating the removal of DI water and ethanol. The rest of the weight loss occurred roughly between 350-450C, indicating endothermic decomposition of DISPERBYK-2018.

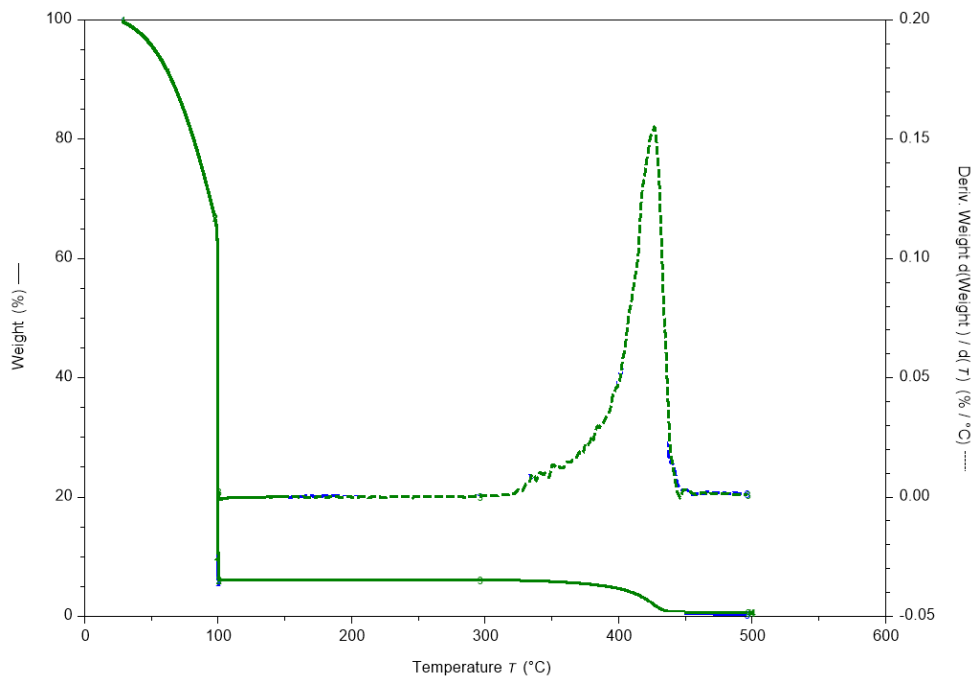


Figure 24. DSC (dashed curve) and TG (solid curve) results obtained using the Si-NP containing ink.

4. Parameter Optimization of 316L in HAMR2

In addition to the hybrid inkjet-SLM system, work was done to characterize and qualify another custom made SLM machine dubbed HAMR2. The bulk of the characterization work was centered around performing parameter sweeps in an attempt to figure out what settings resulted in fully dense parts as well as what might cause lack of fusion or keyholing defects in parts.

4.1. Background & Normalized Enthalpy

The bulk of metal AM processes (SLS, DED, SLM, etc) are just complicated thermal/energy management problems. SLM printing consists of a large number of different parameters that either directly or indirectly affect how energy is delivered and moves throughout a print, and thus the resulting quality of the print [46].

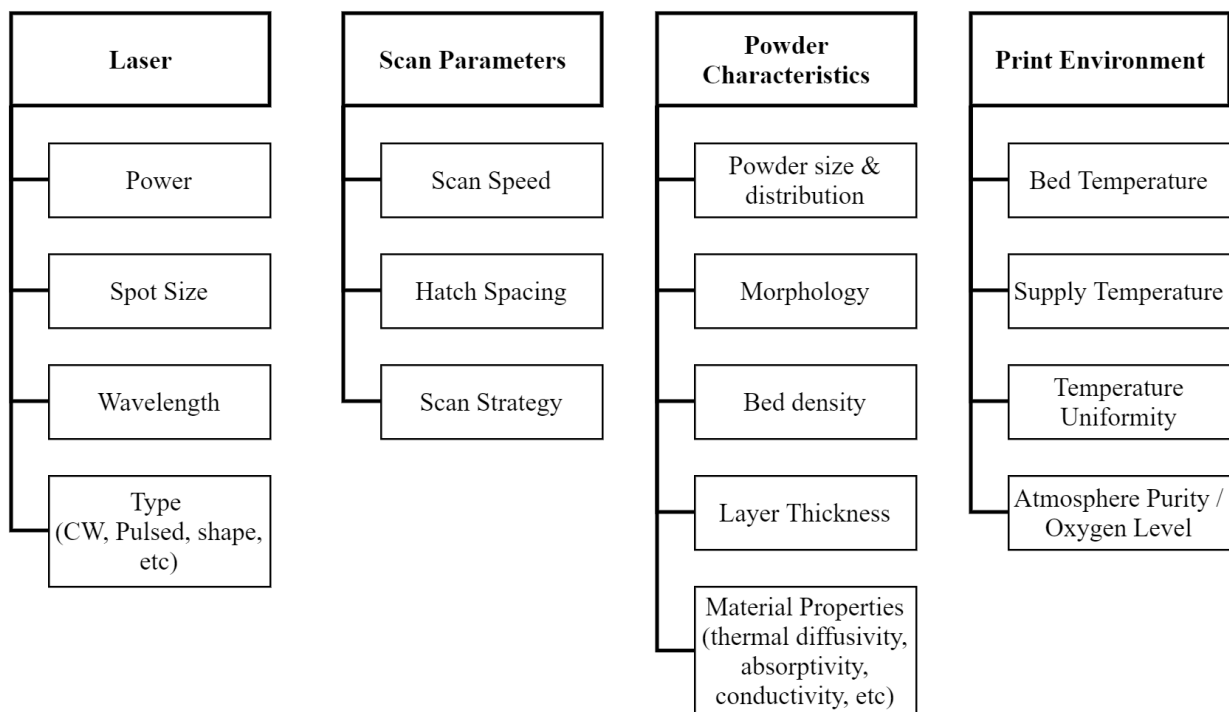


Figure 25. Main process parameters affecting print quality in an SLM system. Adapted from [73].

In the realm of metal AM “optimal” parameters and part quality are typically tied to the printed part’s final density. Other aspects of the part such as its residual stress level, microstructure, and print time and energy are also important but porosities within the part are often the biggest determinant of their overall mechanical strength and fatigue properties [73].

Printed parts may undergo processes like hot isostatic pressing (HIP) in order to mitigate porosities, though even after significant added expenses the prints are likely to still contain pores and generally exhibit poor mechanical properties relative to cast or forged parts in the same material [74], [75].

Scores of papers, simulations, and experiments have been conducted in an attempt to study optimal parameter sets in metal AM. This paper will not dive into the finer details of defect formation and how each parameter within an SLM process influences these mechanisms, though references [76]–[82] offer a general background in the subject. Instead only two main defects will receive focus: lack of fusion and keyholing porosities. The former is typically due to depositing too little energy/heat to the powder bed such that the powder does not completely melt and adhere to itself or the previous layer. Keyholing is typically where too much energy is deposited, forming a deeper than necessary melt pool and vaporizing some of the powder/melt pool in the process. Some of the bubbles formed from the vaporized material then become trapped in the melt pool as it quickly solidifies, forming a pore.

In order to streamline finding the optimal print parameters for new and different materials in different SLM setups, a number of rules and experiments have been performed in the past decade. One method of prominence is appropriately dubbed Volumetric Energy Density (VED) and shown in Eq (1). VED involves the laser power P , scan speed V , layer thickness t , and hatch spacing h .

$$VED = \frac{P}{V t h} \quad (1)$$

VED is meant to be used as a measure of the total energy input into a print (in J/mm³). Though it tends to depend on the material and setup used, a VED of around 100 has been shown to be near optimal (neither resulting in lack of fusion nor too much keyholing) in several scenarios [83], [84]. VED does not consider the various material properties of the powder used or some of the laser parameters though and has thus been generally limited as an effective rule for generating and transferring optimal parameters. Another recently developed method, and the one that this work will focus on, is normalized enthalpy (NE). The equation is presented in Eq (2).

$$\overline{\Delta H} = \frac{\alpha P}{\rho(C\Delta T + L_m)\sqrt{\pi\omega^2 V D}} \quad (2)$$

Where α , ρ , C , L_m , D , are the absorptivity (at the laser's wavelength), density, specific heat, latent heat of melting, and thermal diffusivity of the powder. P , V , ΔT , and ω are the laser power, laser scan speed, the difference between the initial and melting temperature, and the laser spot radius. Several of the material parameters will vary with powder morphology and temperature (namely absorptivity and diffusivity), and so a more rigorous usage of NE would involve finding these values either empirically or experimentally and calculating an effective value for them [85].

4.2. Setup & Experimental Overview

The system to be characterized was another custom SLM printer dubbed HAMR2, which utilizes the same optics as described in Section 2.1 as well as work done by Griggs et al in [68].

Table 4. HAMR2 Capabilities & Parameters

Parameter	Design Values
Spreader type	Compliant blade
Spreader traverse speed	100mm/s
Powder dispensing mechanism	Piston
Build Temperature	20C
Build Volume	75 x 75 x 50 mm
Laser Power	50-550 W
Laser Wavelength	1064nm
Laser Spot Size	>30 μ m (4 σ diameter, adjustable)

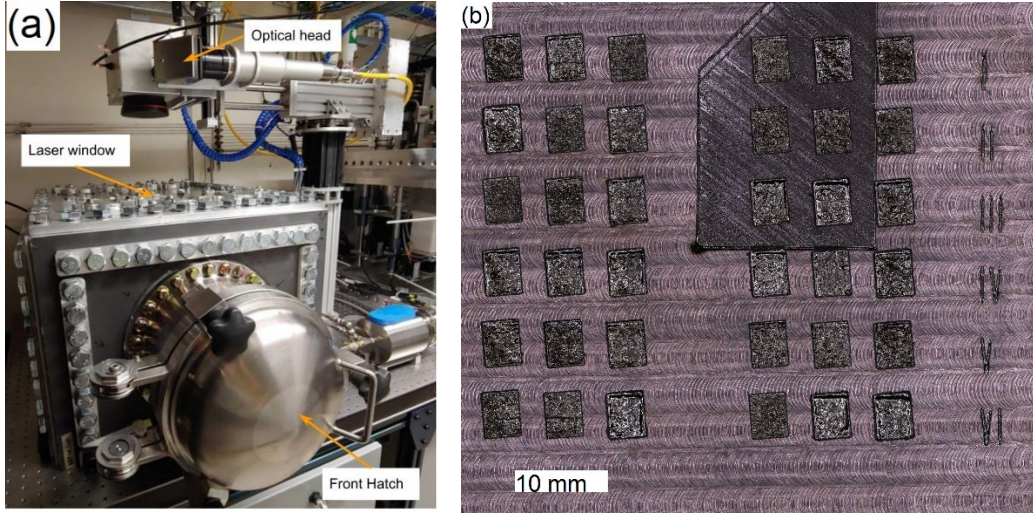


Figure 26. (a) Front view of the HAMR2 SLM machine with the optical head in position over the laser window in the top of the enclosure. (b) Top view of an example print with 36 samples/prisms for parameter optimization. The rastered trapezoid was from a previous test raster.

A spot size of $70\mu\text{m}$ was used for all of the prints. Prior to printing, the enclosure was pumped down and filled with argon until the concentration of oxygen was below 500ppm. For each parameter set a small rectangular prism (roughly 4mm wide, 5mm long, and 2-3mm tall) was printed, and between 4-6 trials of each parameter set were taken (4-6 prisms with the same parameters). A typical print consisted of 36 prisms spaced at least 2.5mm apart. For each print, only the speed, power, and layer heights were varied. All other parameters were kept constant, the speed and power were varied such that certain NEs were achieved spanning from 10-50. It has been shown that an optimal NE typically falls around 25-30 though a sweep of values from 10-50 was used here to both find an optimal point as well as figure out where the bounds for both lack of fusion and keyholing lie for the system [85]. For all prints 316L stainless steel powder from Carpenter (Cartech Micromelt 316L) with a size distribution of $15\text{-}45 \mu\text{m}$ was used. The scan pattern employed for every layer is a simple raster with each line lased consecutively from one side of the prism to the other. Each layer's lines/raster was offset from the previous by 67 degrees.

Table 5. Parameters used and varied during the optimization process

Print Parameter	Value(s)
Spot Size	$70 \mu\text{m}$
Hatch Spacing	$50 \mu\text{m}$
Layer Height	30 or $50 \mu\text{m}$

Speed	250, 500, or 1000 mm/s
Power	(Set based on desired NE)
Normalized Enthalphy (NE)	10, 20, 30, 35, 40, 45, or 50
Powder Used	15-45 μ m 316L Stainless Steel

In order to minimize any effect that a sample's position on the build plate may have on its end quality (i.e. due to spatter from neighboring samples, variations in the recoater, or any aberrations/directionality in the optical system), each parameter set was assigned a random number that determined its index on the build plate. After printing, Reimar Weißbach painstakingly cross sectioned, mounted, polished, and etched each sample such that each sample's porosity and microstructure could be assessed.

4.3. Optimization Process & Results

In order to quickly obtain porosity data, images were taken of each sample's cross section using an optical microscope and processed to gain a proxy measurement. The processing for each image consisted of cropping the image so that only the center of the printed material was included (and none of the baseplate, sides, or top), increasing the contrast, applying a gaussian blur, and then thresholding. The contrast adjustment and gaussian blur both made the pores a little more distinct from the bulk substrate and smoothed over the grain boundaries present after etching so that they would not be picked up in the thresholding. The thresholding limit was set just by taking the minimum pixel intensity and adding a margin to it.

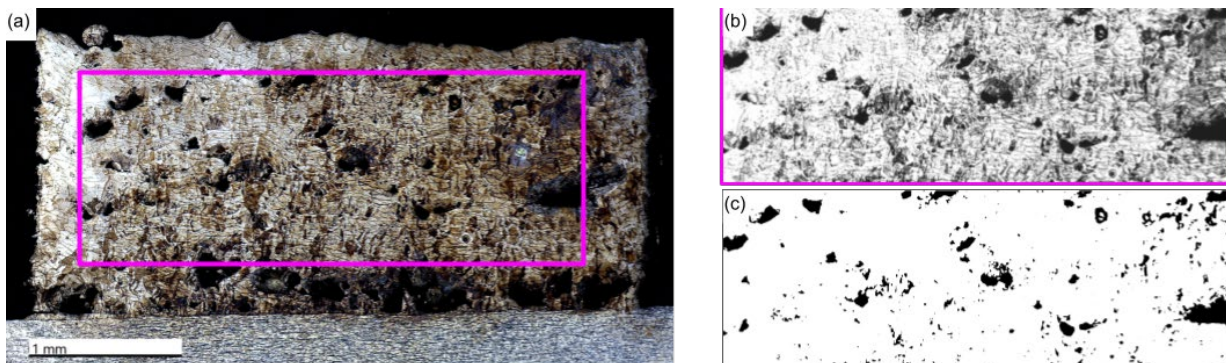


Figure 27. Overview of image processing sequence. (a) is the initial image with the cropped area highlighted by the pink rectangle. (b) is the portion cropped from the original image after converting it to greyscale, increasing the brightness and contrast, and applying a gaussian blur. (c) is the processed image after thresholding.

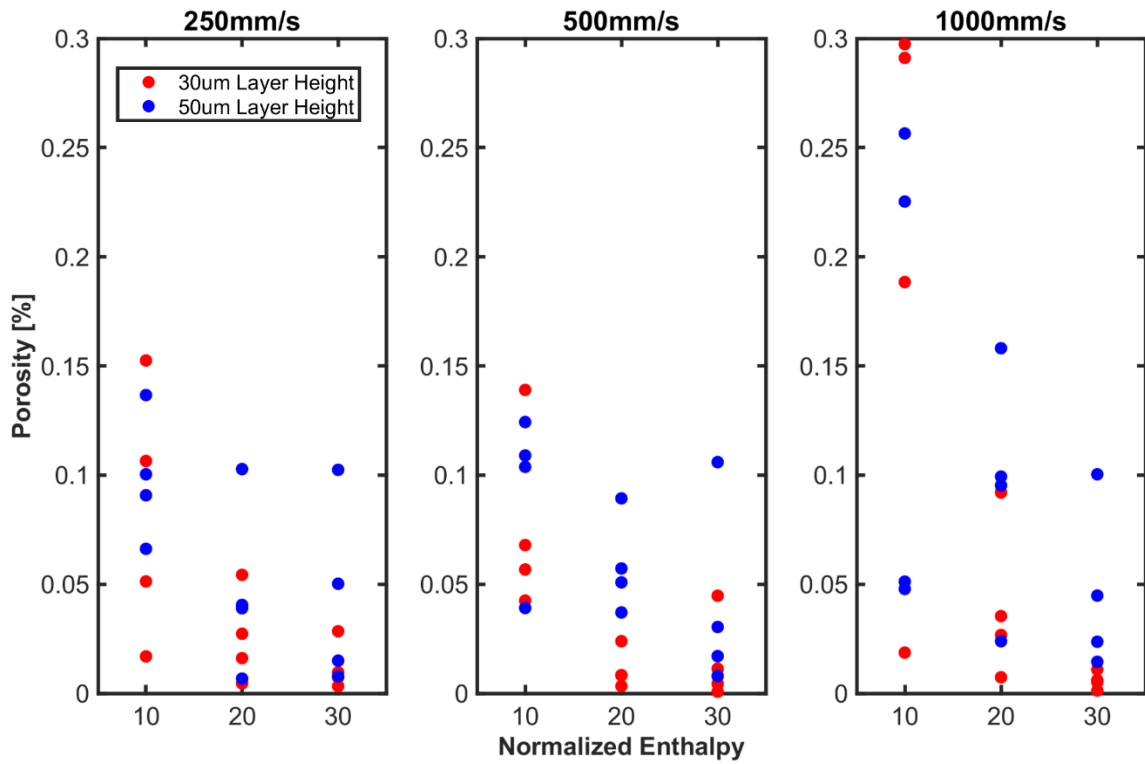


Figure 28. Porosity proxy measurement across different normalized enthalpies, scan speeds, and layer heights.

Further work should be done to continue characterizing prints past NEs of 30 such that there's confidence in an optimal operating parameter set and/or so the keyholing regime for this material and setup may be found.

5. Conclusion

The design and preliminary validation of a hybrid inkjet-LPBF printer was presented throughout this work, along with a brief investigation of inkjet deposition onto a high temperature substrate and a portion of the print parameter sweep and selection for a baseline LPBF machine. Some movement precision data and sample inkjet depositions are shown for the hybrid system.

Some future work on the system may include:

1. Fully verifying and optimizing its precision and functionality. I.e. its bed heater is not fully validated and its control paradigm could likely use tuning.
2. Investigating ink formulations that would survive deposition on substrates over 250C
3. Reworking the printhead to include a multitude of nozzles. This would potentially increase the printer's build speed, enable multiple alloying elements to be deposited, and lower the risk of a single nozzle clogging.
4. The entire system could also be scrapped, and instead a semi-custom/commercial inkjet system could be jammed into a commercial LPBF system. This would likely be far better in terms of part quality and usability.

A. Laser Focusing & Alignment

A1. Laser Focusing

The spot size is variable and is highly sensitive to the height between the f-theta lens and the build surface. The f-theta lens focuses the incoming laser from a ~19.5mm diameter beam (where diameter here refers to the 4σ diameter since it is a gaussian beam) down to a minimum/waist diameter of $\sim 30\mu\text{m}$. The beam decreases in diameter in a nearly linear/conic fashion until it nears its waist, where the spot size shares a very nonlinear/hyperboloid relation with the distance from the lens [86]. In order to accurately set the spot size, an image sensor (DMM 37UX226-ML with $1.85\mu\text{m} \times 1.85\mu\text{m}$ pixels) was placed level with the build surface and exposed to short bursts (2-4 seconds) from the laser/optical head. The laser energy was attenuated by diverting $\sim 95\%$ of it to a beam dump and adding additional neutral density filters inline. This attenuation was performed upstream of the galvanometers and f-theta lens to mitigate any effect they might have on the spot size.

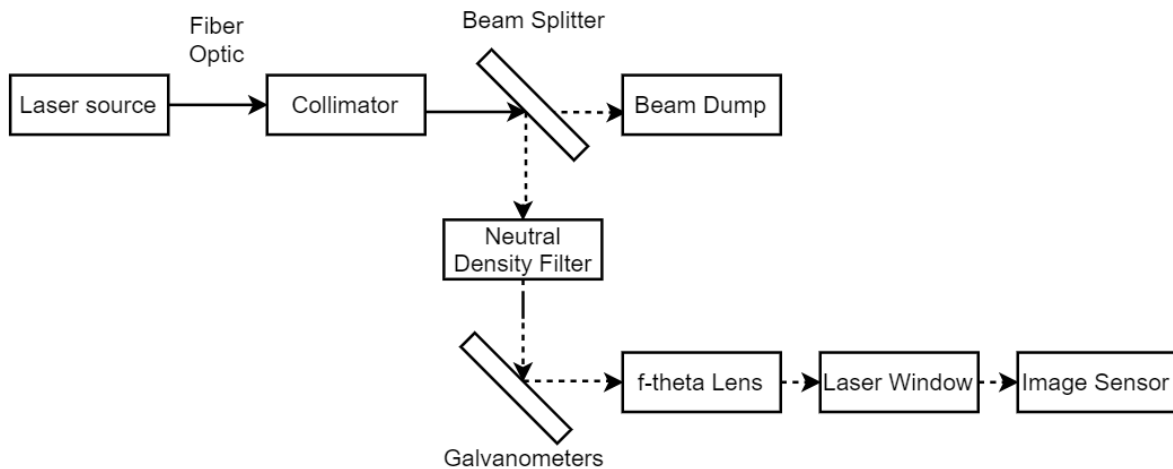


Figure 29. Optical pathway setup for laser focusing & spot size characterization.

The resulting images were then analyzed such that a few gaussian distributions could be fit to the resulting intensity profile and averaged to get a 4σ spot diameter.

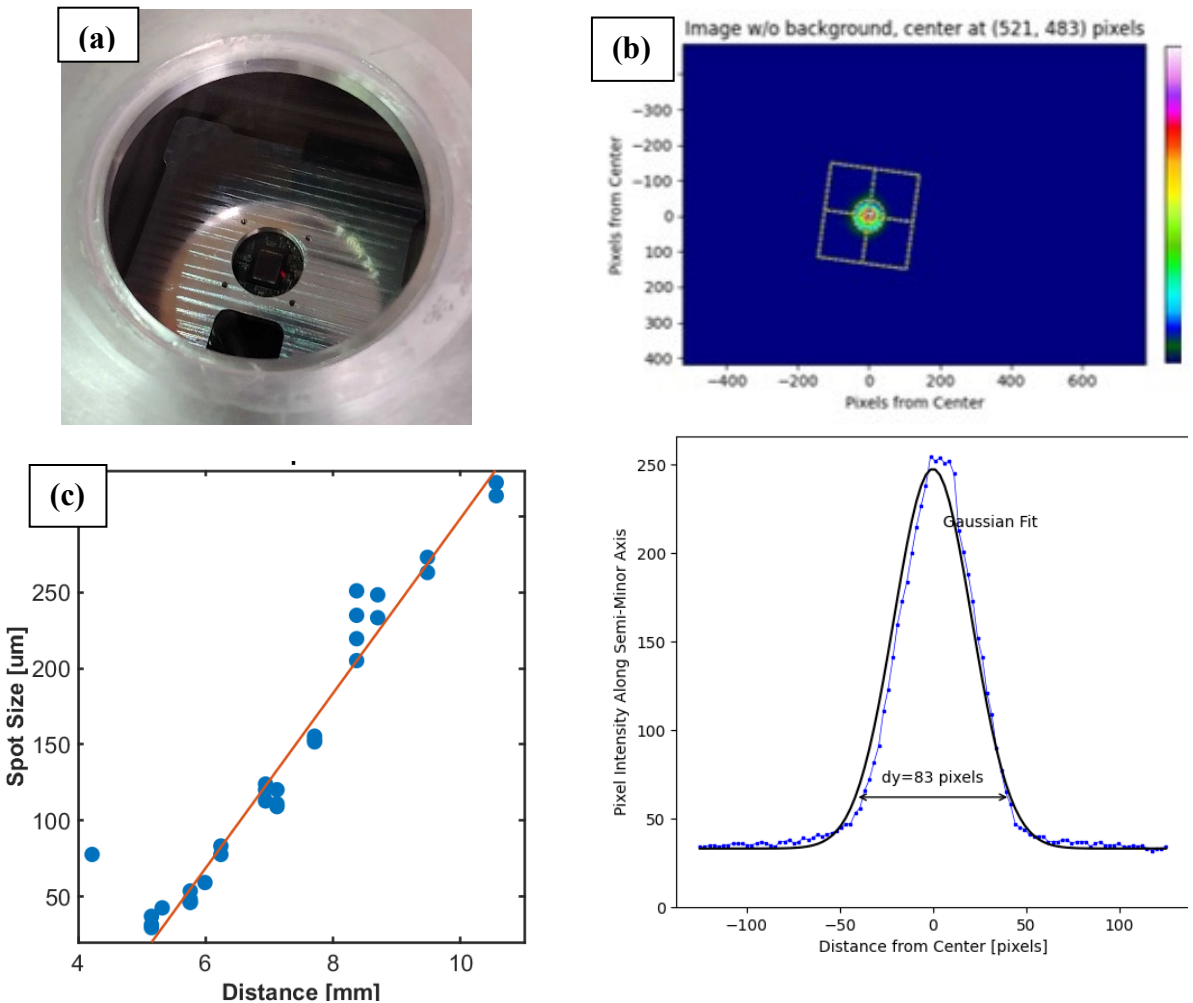


Figure 30. (a) Image sensor in HAMR2 chamber; (b) analyzed image with gaussian fit on the spot; (c) resulting spot size data for HAMR3 with a line of best fit attached.

A2. Laser Alignment

The beam entering the optical head should hit the galvanometer mirrors at the right angle such that when it enters/exits the f-theta lens it doesn't become defocused. The collimator in Figure 29 is attached to an XY stage, and normally directs the laser to a turning mirror whose mount includes two angular adjustments. This yields 4 adjustment points for adjusting the beam angle and point of impact on the galvanometers. In order to align the beam, a set of cameras and a beam splitter was put in place of the f-theta lens. A calibration beam is recorded on the image sensors to provide a "straight" beam for comparison. The cameras were placed different distances from the beam splitter (l_1 & l_2) and a translational/angular error of the incoming beam yields two distinct errors (ε_1 & ε_2) that may be used to both find a rough maximum angular error present in the beam as well as guide optimization of the 4 adjustment points.

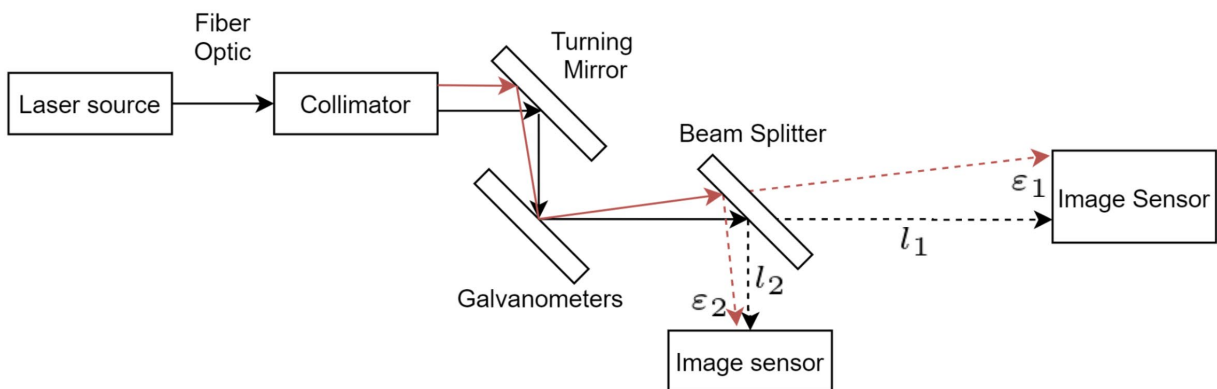


Figure 31. Optical pathway for aligning the incoming beam to the galvanometers.

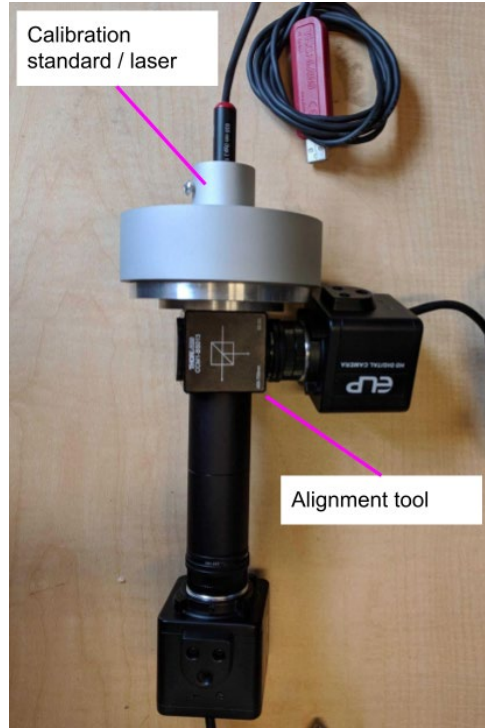


Figure 32. Optical head alignment tool with calibration laser attached.

Bibliography

- [1] I. Gibson, D. Rosen, B. Stucker, and M. Khorasani, “Powder Bed Fusion,” in *Additive Manufacturing Technologies*, I. Gibson, D. Rosen, B. Stucker, and M. Khorasani, Eds., Cham: Springer International Publishing, 2021, pp. 125–170. doi: 10.1007/978-3-030-56127-7_5.
- [2] S. Sun, M. Brandt, and M. Easton, “2 - Powder bed fusion processes: An overview,” in *Laser Additive Manufacturing*, M. Brandt, Ed., in Woodhead Publishing Series in Electronic and Optical Materials. Woodhead Publishing, 2017, pp. 55–77. doi: 10.1016/B978-0-08-100433-3.00002-6.
- [3] M. Ziaee and N. B. Crane, “Binder jetting: A review of process, materials, and methods,” *Additive Manufacturing*, vol. 28, pp. 781–801, Aug. 2019, doi: 10.1016/j.addma.2019.05.031.
- [4] M. Li, W. Du, A. Elwany, Z. Pei, and C. Ma, “Metal Binder Jetting Additive Manufacturing: A Literature Review,” *Journal of Manufacturing Science and Engineering*, vol. 142, no. 9, Jun. 2020, doi: 10.1115/1.4047430.
- [5] A. Mostafaei *et al.*, “Binder jet 3D printing—Process parameters, materials, properties, modeling, and challenges,” *Progress in Materials Science*, vol. 119, p. 100707, Jun. 2021, doi: 10.1016/j.pmatsci.2020.100707.
- [6] D. Metal, “Live Sinter,” *Desktop Metal*. <https://www.desktopmetal.com/resources/live-sinter> (accessed Feb. 20, 2023).
- [7] D.-G. Ahn, “Directed Energy Deposition (DED) Process: State of the Art,” *Int. J. of Precis. Eng. and Manuf.-Green Tech.*, vol. 8, no. 2, pp. 703–742, Mar. 2021, doi: 10.1007/s40684-020-00302-7.
- [8] I. Gibson, D. Rosen, and B. Stucker, “Directed Energy Deposition Processes,” in *Additive Manufacturing Technologies: 3D Printing, Rapid Prototyping, and Direct Digital Manufacturing*, I. Gibson, D. Rosen, and B. Stucker, Eds., New York, NY: Springer, 2015, pp. 245–268. doi: 10.1007/978-1-4939-2113-3_10.
- [9] S.-H. Li, P. Kumar, S. Chandra, and U. Ramamurty, “Directed energy deposition of metals: processing, microstructures, and mechanical properties,” *International Materials Reviews*, vol. 0, no. 0, pp. 1–43, Jul. 2022, doi: 10.1080/09506608.2022.2097411.
- [10] C. Y. Yap *et al.*, “Review of selective laser melting: Materials and applications,” *Applied Physics Reviews*, vol. 2, no. 4, p. 041101, Dec. 2015, doi: 10.1063/1.4935926.
- [11] X. Zhang, C. J. Yocom, B. Mao, and Y. Liao, “Microstructure evolution during selective laser melting of metallic materials: A review,” *Journal of Laser Applications*, vol. 31, no. 3, p. 031201, Aug. 2019, doi: 10.2351/1.5085206.
- [12] P. Konda Gokuldoss, S. Kolla, and J. Eckert, “Additive Manufacturing Processes: Selective Laser Melting, Electron Beam Melting and Binder Jetting—Selection Guidelines,” *Materials (Basel)*, vol. 10, no. 6, p. 672, Jun. 2017, doi: 10.3390/ma10060672.
- [13] S. Gruber *et al.*, “Comparison of dimensional accuracy and tolerances of powder bed based and nozzle based additive manufacturing processes,” *Journal of Laser Applications*, vol. 32, 2020, doi: <https://doi.org/10.2351/7.0000115>.
- [14] H. Kalman, A. Satran, D. Meir, and E. Rabinovich, “Pickup (critical) velocity of particles,” *Powder Technology*, vol. 160, no. 2, pp. 103–113, Dec. 2005, doi: 10.1016/j.powtec.2005.08.009.

- [15] J. Reijonen, A. Revuelta, T. Riipinen, K. Ruusuvuori, and P. Puukko, “On the effect of shielding gas flow on porosity and melt pool geometry in laser powder bed fusion additive manufacturing,” *Additive Manufacturing*, vol. 32, p. 101030, Mar. 2020, doi: 10.1016/j.addma.2019.101030.
- [16] B. Ferrar, L. Mullen, E. Jones, R. Stamp, and C. J. Sutcliffe, “Gas flow effects on selective laser melting (SLM) manufacturing performance,” *Journal of Materials Processing Technology*, vol. 212, no. 2, pp. 355–364, Feb. 2012, doi: 10.1016/j.jmatprotec.2011.09.020.
- [17] B. Saleh *et al.*, “30 Years of functionally graded materials: An overview of manufacturing methods, Applications and Future Challenges,” *Composites Part B: Engineering*, vol. 201, p. 108376, Nov. 2020, doi: 10.1016/j.compositesb.2020.108376.
- [18] C. Zhang *et al.*, “Additive manufacturing of functionally graded materials: A review,” *Materials Science and Engineering: A*, vol. 764, p. 138209, Sep. 2019, doi: 10.1016/j.msea.2019.138209.
- [19] G. H. Loh, E. Pei, D. Harrison, and M. D. Monzón, “An overview of functionally graded additive manufacturing,” *Additive Manufacturing*, vol. 23, pp. 34–44, Oct. 2018, doi: 10.1016/j.addma.2018.06.023.
- [20] B. Zhang, P. Jaiswal, R. Rai, and S. Nelaturi, “Additive Manufacturing of Functionally Graded Material Objects: A Review,” *Journal of Computing and Information Science in Engineering*, vol. 18, no. 4, Jul. 2018, doi: 10.1115/1.4039683.
- [21] A. Reichardt *et al.*, “Advances in additive manufacturing of metal-based functionally graded materials,” *International Materials Reviews*, vol. 66, no. 1, pp. 1–29, Jan. 2021, doi: 10.1080/09506608.2019.1709354.
- [22] I. M. El-Galy, B. I. Saleh, and M. H. Ahmed, “Functionally graded materials classifications and development trends from industrial point of view,” *SN Appl. Sci.*, vol. 1, no. 11, p. 1378, Oct. 2019, doi: 10.1007/s42452-019-1413-4.
- [23] W. Pompe *et al.*, “Functionally graded materials for biomedical applications,” *Materials Science and Engineering: A*, vol. 362, no. 1, pp. 40–60, Dec. 2003, doi: 10.1016/S0921-5093(03)00580-X.
- [24] E. Müller, Č. Drašar, J. Schilz, and W. A. Kaysser, “Functionally graded materials for sensor and energy applications,” *Materials Science and Engineering: A*, vol. 362, no. 1, pp. 17–39, Dec. 2003, doi: 10.1016/S0921-5093(03)00581-1.
- [25] V. Stathopoulos *et al.*, “Design of functionally graded multilayer thermal barrier coatings for gas turbine application,” *Surface and Coatings Technology*, vol. 295, pp. 20–28, Jun. 2016, doi: 10.1016/j.surfcoat.2015.11.054.
- [26] L. V. Ramanathan, “Challenges in oxidation resistant coatings,” *Surface Engineering*, vol. 23, no. 4, pp. 239–242, Jul. 2007, doi: 10.1179/174329407X245066.
- [27] D. Oropeza, S. Firdosy, and D. C. Hofmann, “Development of in-plane SS316 to M300 maraging steel gradients via directed energy deposition,” *Additive Manufacturing Letters*, vol. 3, p. 100078, Dec. 2022, doi: 10.1016/j.addlet.2022.100078.
- [28] J. P. Kelly, J. W. Elmer, F. J. Ryerson, J. R. I. Lee, and J. J. Haslam, “Directed energy deposition additive manufacturing of functionally graded Al-W composites,” *Additive Manufacturing*, vol. 39, p. 101845, Mar. 2021, doi: 10.1016/j.addma.2021.101845.
- [29] S. Gruber *et al.*, “Comparison of dimensional accuracy and tolerances of powder bed based and nozzle based additive manufacturing processes,” *Journal of Laser Applications*, vol. 32, no. 3, p. 032016, Aug. 2020, doi: 10.2351/7.0000115.

- [30] A. G. Demir *et al.*, “Enabling multi-material gradient structure in laser powder bed fusion,” *Journal of Materials Processing Technology*, vol. 301, p. 117439, Mar. 2022, doi: 10.1016/j.jmatprotec.2021.117439.
- [31] “How Selective Powder Deposition Works,” 2022. <https://iro3d.com/> (accessed Nov. 26, 2022).
- [32] Aerosint, “Tool-free metal and ceramic forming with dies printed on-the-fly,” *Medium*, Jan. 07, 2020. <https://medium.com/@aerosint/tool-free-metal-and-ceramic-forming-with-dies-printed-on-the-fly-ff75579d38b9> (accessed Nov. 26, 2022).
- [33] J. Walker, J. R. Middendorf, C. C. C. Lesko, and J. Gockel, “Multi-material laser powder bed fusion additive manufacturing in 3-dimensions,” *Manufacturing Letters*, vol. 31, pp. 74–77, Jan. 2022, doi: 10.1016/j.mfglet.2021.07.011.
- [34] H. F. Abutarboush, “Silver nanoparticle inkjet-printed multiband antenna on synthetic paper material for flexible devices,” *Alexandria Engineering Journal*, vol. 61, pp. 6349–6355, 2022, doi: 10.1016/J.AEJ.2021.11.060.
- [35] T. Öhlund, J. Örtегren, S. Forsberg, and H. E. Nilsson, “Paper surfaces for metal nanoparticle inkjet printing,” *Appl Surf Sci*, vol. 259, pp. 731–739, 2012, doi: 10.1016/J.APSUSC.2012.07.112.
- [36] S. K. Tam, K. Y. Fung, G. S. H. Poon, and K. M. Ng, “Product design: Metal nanoparticle-based conductive inkjet inks,” *AICHE Journal*, vol. 62, no. 8, pp. 2740–2753, 2016, doi: 10.1002/aic.15271.
- [37] J. Stringer *et al.*, “Integration of additive manufacturing and inkjet printed electronics: a potential route to parts with embedded multifunctionality,” *Manufacturing Review*, vol. 3, Jul. 2016, Accessed: Nov. 26, 2022. [Online]. Available: <https://doi.org/10.1051/mfreview/2016011>
- [38] Y. Guo, H. S. Patanwala, B. Bognet, and A. W. K. Ma, “Inkjet and inkjet-based 3D printing: connecting fluid properties and printing performance,” *Rapid Prototyping Journal*, vol. 23, no. 3, pp. 562–576, Jan. 2017, doi: 10.1108/RPJ-05-2016-0076.
- [39] M. Rafiq *et al.*, “Overview of printable nanoparticles through inkjet process: Their application towards medical use,” *Microelectron Eng*, vol. 266, p. 111889, 2022, doi: 10.1016/J.MEE.2022.111889.
- [40] O. Brand, G. K. Fedder, C. Hierold, J. G. Korvink, and O. Tabata, *Inkjet-based Micromanufacturing*. John Wiley & Sons, 2012.
- [41] S. D. Hoath, *Fundamentals of Inkjet Printing: The Science of Inkjet and Droplets*. John Wiley & Sons, 2016.
- [42] D. Oropeza and A. J. Hart, “A laboratory-scale binder jet additive manufacturing testbed for process exploration and material development,” *Int J Adv Manuf Technol*, vol. 114, no. 11, pp. 3459–3473, Jun. 2021, doi: 10.1007/s00170-021-07123-1.
- [43] R. Waasdorp, O. van den Heuvel, F. Versluis, B. Hajee, and M. Krishna Ghatkesar, “Accessing individual 75-micron diameter nozzles of a desktop inkjet printer to dispense picoliter droplets on demand,” *RSC Advances*, vol. 8, no. 27, pp. 14765–14774, 2018, doi: 10.1039/C8RA00756J.
- [44] E. Saleh *et al.*, “3D Inkjet Printing of Electronics Using UV Conversion,” *Advanced Materials Technologies*, vol. 2, no. 10, p. 1700134, 2017, doi: 10.1002/admt.201700134.
- [45] S. Ko, J. Chung, N. Hotz, K. Nam, and C. P. Grigoropoulos, “Metal nanoparticle direct inkjet printing for low-temperature 3D micro metal structure fabrication - IOPscience,” *Journal of Micromechanics and Microengineering*, vol. 20, p. 125010, 2010.

- [46] C. Meier, R. W. Penny, Y. Zou, J. S. Gibbs, and A. J. Hart, “Thermophysical Phenomena in Metal Additive Manufacturing by Selective Laser Melting: Fundamentals, Modeling, Simulation and Experimentation,” *Annual Rev Heat Transfer*, vol. 20, no. 1, pp. 241–316, 2017, doi: 10.1615/AnnualRevHeatTransfer.2018019042.
- [47] R. Mertens, B. Vrancken, N. Holmstock, Y. Kinds, J.-P. Kruth, and J. Van Humbeeck, “Influence of Powder Bed Preheating on Microstructure and Mechanical Properties of H13 Tool Steel SLM Parts,” *Physics Procedia*, vol. 83, pp. 882–890, Jan. 2016, doi: 10.1016/j.phpro.2016.08.092.
- [48] R. Mertens, S. Dadbakhsh, J. V. Humbeeck, and J.-P. Kruth, “Application of base plate preheating during selective laser melting,” *Procedia CIRP*, vol. 74, pp. 5–11, Jan. 2018, doi: 10.1016/j.procir.2018.08.002.
- [49] R. Grill and A. Gnadenberger, “Niobium as mint metal: Production–properties–processing,” *Int J Refract Metals Hard Mater*, vol. 24, pp. 275–282, 2006, doi: 10.1016/J.IJRMHM.2005.10.008.
- [50] I. T. Hong and C. H. Koo, “The study of vacuum-furnace brazing of C103 and Ti–6Al–4V using Ti–15Cu–15Ni foil,” *Mater Chem Phys*, vol. 94, pp. 131–140, 2005, doi: 10.1016/J.MATCHEMPHYS.2005.04.021.
- [51] P. Mastanaiah, G. M. Reddy, K. S. Prasad, and C. V. S. Murthy, “An investigation on microstructures and mechanical properties of explosive cladded C103 niobium alloy over C263 nimonic alloy,” *J Mater Process Technol*, vol. 214, pp. 2316–2324, 2014, doi: 10.1016/J.JMATPROTEC.2014.04.025.
- [52] J. Chen *et al.*, “Laser powder bed fusion of a Nb-based refractory alloy: Microstructure and tensile properties,” *Materials Science and Engineering: A*, vol. 843, p. 143153, 2022, doi: 10.1016/J.MSEA.2022.143153.
- [53] Y. Guo, L. Jia, B. Kong, F. Zhang, J. Liu, and H. Zhang, “Improvement in the oxidation resistance of Nb-Si based alloy by selective laser melting,” *Corros Sci*, vol. 127, pp. 260–269, 2017, doi: 10.1016/J.CORSCI.2017.08.022.
- [54] C. A. Terrazas *et al.*, “Fabrication and characterization of high-purity niobium using electron beam melting additive manufacturing technology,” *The International Journal of Advanced Manufacturing Technology*, vol. 84, no. 5, pp. 1115–1126, 2015, doi: 10.1007/S00170-015-7767-X.
- [55] Z. Sun, F. Bao, F. Zhang, Y. Li, M. Wang, and X. Guo, “Effect of TiC on microstructures and mechanical behaviors of low-density Nb-Ti-Al alloys fabricated by laser solid forming,” *Int J Refract Metals Hard Mater*, vol. 108, p. 105955, 2022, doi: 10.1016/J.IJRMHM.2022.105955.
- [56] Y. Guo, L. Jia, B. Kong, S. Zhang, F. Zhang, and H. Zhang, “Microstructure of rapidly solidified Nb-based pre-alloyed powders for additive manufacturing,” *Appl Surf Sci*, vol. 409, pp. 367–374, 2017, doi: 10.1016/J.APSUSC.2017.02.221.
- [57] P. D. Awasthi *et al.*, “Mechanical properties and microstructural characteristics of additively manufactured C103 niobium alloy,” *Materials Science and Engineering: A*, vol. 831, p. 142183, 2022, doi: 10.1016/J.MSEA.2021.142183.
- [58] N. R. Philips, M. Carl, and N. J. Cunningham, “New Opportunities in Refractory Alloys,” *Metall Mater Trans A Phys Metall Mater Sci*, vol. 51, pp. 3299–3310, 2020, doi: 10.1007/S11661-020-05803-3/FIGURES/10.

- [59] B. Vrancken, W. E. King, and M. J. Matthews, “In-situ characterization of tungsten microcracking in Selective Laser Melting,” *Procedia CIRP*, vol. 74, pp. 107–110, 2018, doi: 10.1016/J.PROCIR.2018.08.050.
- [60] G. Marinelli, F. Martina, H. Lewtas, D. Hancock, S. Ganguly, and S. Williams, “Functionally graded structures of refractory metals by wire arc additive manufacturing,” *Https://Doi.Org/10.1080/13621718.2019.1586162*, vol. 24, pp. 495–503, 2019, doi: 10.1080/13621718.2019.1586162.
- [61] J. Braun *et al.*, “Molybdenum and tungsten manufactured by selective laser melting: Analysis of defect structure and solidification mechanisms,” *International Journal of Refractory Metals and Hard Materials*, vol. 84, p. 104999, Nov. 2019, doi: 10.1016/j.ijrmhm.2019.104999.
- [62] H. Dobbelstein, M. Thiele, E. L. Gurevich, E. P. George, and A. Ostendorf, “Direct Metal Deposition of Refractory High Entropy Alloy MoNbTaW,” *Physics Procedia*, vol. 83, pp. 624–633, Jan. 2016, doi: 10.1016/j.phpro.2016.08.065.
- [63] J. Xue, Z. Feng, J. Tang, C. Tang, and Z. Zhao, “Selective laser melting additive manufacturing of tungsten with niobium alloying: Microstructure and suppression mechanism of microcracks,” *Journal of Alloys and Compounds*, vol. 874, p. 159879, Sep. 2021, doi: 10.1016/j.jallcom.2021.159879.
- [64] H. P. Tang, G. Y. Yang, W. P. Jia, W. W. He, S. L. Lu, and M. Qian, “Additive manufacturing of a high niobium-containing titanium aluminide alloy by selective electron beam melting,” *Materials Science and Engineering: A*, vol. 636, pp. 103–107, Jun. 2015, doi: 10.1016/j.msea.2015.03.079.
- [65] D. Quéré, “Leidenfrost Dynamics,” *Annu. Rev. Fluid Mech.*, vol. 45, no. 1, pp. 197–215, Jan. 2013, doi: 10.1146/annurev-fluid-011212-140709.
- [66] B. Sobac, A. Rednikov, S. Dorbolo, and P. Colinet, “Chapter 7 - Leidenfrost Drops,” in *Droplet Wetting and Evaporation*, D. Brutin, Ed., Oxford: Academic Press, 2015, pp. 85–99. doi: 10.1016/B978-0-12-800722-8.00007-2.
- [67] J. D. Bernardin and I. Mudawar, “The Leidenfrost Point: Experimental Study and Assessment of Existing Models,” *Journal of Heat Transfer*, vol. 121, no. 4, pp. 894–903, Nov. 1999, doi: 10.1115/1.2826080.
- [68] D. A. Griggs, J. S. Gibbs, S. P. Baker, R. W. Penny, M. C. Feldmann, and A. J. Hart, “A Testbed for Investigation of Selective Laser Melting at Elevated Atmospheric Pressure.” arXiv, Jul. 04, 2021. doi: 10.48550/arXiv.2107.01744.
- [69] “Special Metals INCONEL® Alloy 625.” <https://www.matweb.com/search/DataSheet.aspx?MatGUID=4a194f59f35a427dbc5009f043349cb5&ckck=1> (accessed Jan. 14, 2023).
- [70] L. Caprio, A. G. Demir, G. Chiari, and B. Previtali, “Defect-free laser powder bed fusion of Ti–48Al–2Cr–2Nb with a high temperature inductive preheating system,” *J. Phys. Photonics*, vol. 2, no. 2, p. 024001, Feb. 2020, doi: 10.1088/2515-7647/ab7080.
- [71] “Cyclone design - Step by step guide - Powderprocess.net.” https://powderprocess.net/Equipments%20html/Cyclone_Design.html (accessed Mar. 26, 2023).
- [72] S. Abbott, *Printing Science: Principles and Practice*. 2018.
- [73] S. Wang *et al.*, “Role of porosity defects in metal 3D printing: Formation mechanisms, impacts on properties and mitigation strategies,” *Materials Today*, vol. 59, pp. 133–160, Oct. 2022, doi: 10.1016/j.mattod.2022.08.014.

- [74] T. Cegan *et al.*, “Effect of Hot Isostatic Pressing on Porosity and Mechanical Properties of 316 L Stainless Steel Prepared by the Selective Laser Melting Method,” *Materials (Basel)*, vol. 13, no. 19, p. 4377, Oct. 2020, doi: 10.3390/ma13194377.
- [75] M. Khomutov *et al.*, “Effect of hot isostatic pressing on structure and properties of intermetallic NiAl–Cr–Mo alloy produced by selective laser melting,” *Intermetallics*, vol. 120, p. 106766, May 2020, doi: 10.1016/j.intermet.2020.106766.
- [76] E. Liverani, S. Toschi, L. Ceschini, and A. Fortunato, “Effect of selective laser melting (SLM) process parameters on microstructure and mechanical properties of 316L austenitic stainless steel,” *Journal of Materials Processing Technology*, vol. 249, pp. 255–263, Nov. 2017, doi: 10.1016/j.jmatprotec.2017.05.042.
- [77] B. Zhang, Y. Li, and Q. Bai, “Defect Formation Mechanisms in Selective Laser Melting: A Review,” *Chin. J. Mech. Eng.*, vol. 30, no. 3, Art. no. 3, May 2017, doi: 10.1007/s10033-017-0121-5.
- [78] “Optimization of selective laser melting parameters and influence of post heat treatment on microstructure and mechanical properties of maraging steel,” *Materials & Design*, vol. 139, pp. 486–497, Feb. 2018, doi: 10.1016/j.matdes.2017.11.042.
- [79] K. Q. Le, C. Tang, and C. H. Wong, “On the study of keyhole-mode melting in selective laser melting process,” *International Journal of Thermal Sciences*, vol. 145, p. 105992, Nov. 2019, doi: 10.1016/j.ijthermalsci.2019.105992.
- [80] K. Darvish, Z. W. Chen, and T. Pasang, “Reducing lack of fusion during selective laser melting of CoCrMo alloy: Effect of laser power on geometrical features of tracks,” *Materials & Design*, vol. 112, pp. 357–366, Dec. 2016, doi: 10.1016/j.matdes.2016.09.086.
- [81] C. Teng *et al.*, “Simulating Melt Pool Shape and Lack of Fusion Porosity for Selective Laser Melting of Cobalt Chromium Components,” *Journal of Manufacturing Science and Engineering*, vol. 139, Jul. 2016, doi: 10.1115/1.4034137.
- [82] S. Shrestha, T. Starr, and K. Chou, “A Study of Keyhole Porosity in Selective Laser Melting: Single-Track Scanning With Micro-CT Analysis,” *Journal of Manufacturing Science and Engineering*, vol. 141, p. 1, Apr. 2019, doi: 10.1115/1.4043622.
- [83] H. R. Javidrad, M. Ghanbari, and F. Javidrad, “Effect of scanning pattern and volumetric energy density on the properties of selective laser melting Ti-6Al-4V specimens,” *Journal of Materials Research and Technology*, vol. 12, pp. 989–998, May 2021, doi: 10.1016/j.jmrt.2021.03.044.
- [84] U. Scipioni Bertoli, A. J. Wolfer, M. J. Matthews, J.-P. R. Delplanque, and J. M. Schoenung, “On the limitations of Volumetric Energy Density as a design parameter for Selective Laser Melting,” *Materials & Design*, vol. 113, pp. 331–340, Jan. 2017, doi: 10.1016/j.matdes.2016.10.037.
- [85] H. Ghasemi-Tabasi, J. Jhabvala, E. Boillat, T. Ivas, R. Drissi-Daoudi, and R. E. Logé, “An effective rule for translating optimal selective laser melting processing parameters from one material to another,” *Additive Manufacturing*, vol. 36, p. 101496, Dec. 2020, doi: 10.1016/j.addma.2020.101496.
- [86] “Focusing on Laser Melting Performance,” *Renishaw*, 2017.
<https://www.renishaw.com/en/focusing-on-laser-melting-performance--43442>